

Depth to Basement and Geoid Expression of the Kane Fracture Zone: A Comparison

R. DIETMAR MÜLLER^{1,4} DAVID T. SANDWELL², BRIAN E. TUCHOLKE³, JOHN G. SCLATER¹, and PETER R. SHAW³

¹The Department of Geological Sciences, The University of Texas, Austin, TX 78713 and The Institute for Geophysics, The University of Texas, 8701 Mopac Boulevard, Austin, TX 78759, U.S.A. ²Scripps Institution of Oceanography, Geological Research Division, La Jolla, CA 92093, U.S.A. ³Woods Hole Oceanographic Institution, Woods Hole, MA 02543, U.S.A. ⁴Now at Scripps Institution of Oceanography, La Jolla, CA 92093-0208, U.S.A.

(Received 30 June, 1989; in final form 9 May, 1990)

Key words: Geoid topography, fracture zone morphology, satellite altimetry, transform fault, plate reconstructions.

Abstract. Geoid data from Geosat and subsatellite basement depth profiles of the Kane Fracture Zone in the central North Atlantic were used to examine the correlation between the short-wavelength geoid ($\lambda = 25\text{--}100$ km) and the uncompensated basement topography. The processing technique we apply allows the stacking of geoid profiles, although each repeat cycle has an unknown long-wavelength bias. We first formed the derivative of individual profiles, stacked up to 22 repeat cycles, and then integrated the average-slope profile to reconstruct the geoid height. The stacked, filtered geoid profiles have a noise level of about 7 mm in geoid height. The subsatellite basement topography was obtained from a recent compilation of structure contours on basement along the entire length of the Kane Fracture Zone. The ratio of geoid height to topography over the Kane Fracture Zone valley decreases from about $20\text{--}25$ cm km⁻¹ over young ocean crust to $5\text{--}0$ cm km⁻¹ over ocean crust older than 140 Ma. Both geoid and basement depth of profiles were projected perpendicular to the Kane Fracture Zone, resampled at equal intervals and then cross correlated. The cross correlation shows that the short-wavelength geoid height is well correlated with the basement topography. For 33 of the 37 examined profiles, the horizontal mismatches are 10 km or less with an average mismatch of about 5 km. This correlation is quite good considering that the average width of the Kane Fracture Zone valley at median depth is 10–15 km. The remaining four profiles either cross the transverse ridge just east of the active Kane transform zone or overlie old crust of the M-anomaly sequence. The mismatch over the transverse ridge probably is related to a crustal density anomaly. The relatively poor correlation of geoid and basement depth in profiles of ocean crust older than 130–140 Ma reflects poor basement-depth control along subsatellite tracks.

Introduction

Rapid development of remote sensing and data imaging techniques in recent years allows the uni-

form mapping of the geoid over the oceans. High-frequency anomalies in the height of the ocean surface can be used to map linear topographic features on the ocean floor. In order to interpret the location of fracture zones from geoid data as recorded by satellite, the exact correlation between the geoid and the topography of fracture zones must be determined. A generalized model for correlation between geoid, deflection of the vertical and fracture-zone topography (Figure 1) was used by Gahagan *et al.* (1988) to construct a preliminary global tectonic-fabric map of the ocean floor, based on the interpretation of deflection-of-the-vertical data from Seasat and Geosat. Although the tectonic development and the geoid expression of fracture zones in fast-spreading Pacific crust is fairly well understood (Sandwell and Schubert, 1982), no detailed comparison between the topography and geoid of a complete fossil trace of a fracture zone in the Atlantic or Indian Ocean has been reported. Better 'ground truth' for such fracture zones in slow-spreading crust is required if Geosat data are to be used to map the ocean floor in regions where bathymetric data are sparse, such as in remote high southern latitudes.

The relation between geoid, deflection of the vertical, and bathymetry of six fracture zones in the North Pacific was established by Sandwell and Schubert (1982). Their flexure model explains the distinct depth/age step of large-offset Pacific fracture zones in a fast spreading regime (Figure 1). Because of the apparent absence of vertical slip along fault planes of fossil fracture zones, this age/depth step seems often

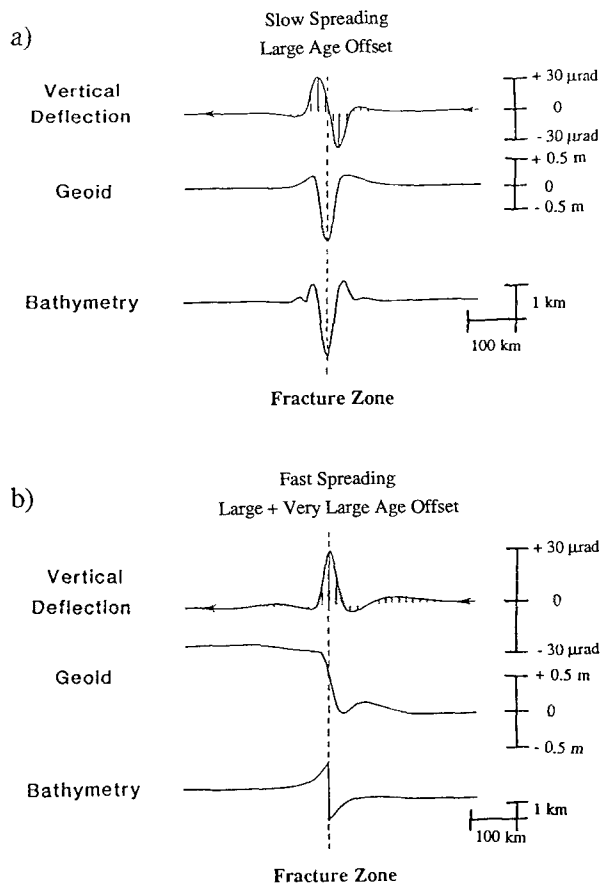


Fig. 1. Relation between geoid, deflection of the vertical, and fracture-zone topography for (a) slow-spreading large-offset and (b) fast-spreading large to very large offset fracture zones.

to be retained even in the oldest parts of the sea floor (Sandwell and Schubert, 1982).

Fracture Zones in slow-spreading regimes (Figure 1), as in the Atlantic and western Indian Ocean, have distinctly different topography. In contrast to the Pacific, Atlantic fracture zones exhibit a more complex morphology (Collette, 1986), and the expected depth/age step commonly is overprinted by the high-amplitude fracture-zone topography (Colette *et al.*, 1984; Colette, 1986; Fox and Gallo, 1986; Potts *et al.*, 1986; Roest and Collette, 1986). A characteristic feature of Atlantic fracture zones is a central trough having a graben-like character (Van Andel, 1971; Fox and Gallo, 1986). Collette (1974) and Turcotte (1974) invoked the concept of thermal contraction of the lithosphere parallel to the spreading axis to explain the existence of such fracture-zone troughs. Francheteau *et al.* (1976), however, pointed out that this mechanism results in too little extension

to be significant. Fox and Gallo (1984) developed a tectonic model that explains the formation of fracture-zone troughs on slow-spreading ridges by a change in isostasy of the lithosphere, which is caused by a change in lithospheric properties (e.g., composition and mass distribution) at ridge-transform intersections.

Three distinctly different types of fracture zones have been identified in slow spreading regimes. Small offsets of the spreading ridge axis less than ca. 20 km (~ 1.5 m.y) are characterized by faults trending 45° – 75° relative to the adjacent spreading axes and exhibit a shallow fracture valley. In contrast, large offsets more than about 30 km (~ 2 m.y.), show a rectilinear system of transform shears and have a well developed transform valley (Macdonald, 1986; Tucholke and Schouten, 1988). The best examples of such large offsets in the North Atlantic are the Oceanographer, Hayes, Atlantis, and Kane fracture zones. There is a third type of fracture zone in slow-spreading ocean crust that displays features of both fast- and slow-spreading large offsets. Very large offset transforms (several hundreds of kilometers) have complex morphologies that combine a depth/age step typical for Pacific-type fracture zones with the Atlantic characteristics of rugged topography and the presence of a central valley. Examples of this type of fracture zone are the Romanche Fracture Zone (offset ~ 900 km), characterized by a depth/age step as well as a large-amplitude topography (Sandwell, 1984), and the Charlie-Gibbs Fracture Zone, which is an unusual double fracture zone with an offset of 350 km (~ 25 m.y.). The Charlie-Gibbs exhibits two parallel east-west trending troughs (Olivet *et al.*, 1974) accompanied overall by a significant depth-age step (GEBCO-Sheet 5.04).

Vogt *et al.* (1984) compared 9300 km of marine geophysical data along suborbital tracks with Seasat data in the central North Atlantic. They showed that there is a good correlation between geoid height, free-air gravity, and seafloor topography, and that grabens along fracture zones usually are accompanied by a geoid low (schematically shown in Figure 1). Roest (1987) also found good correlation between along-track gravity from Seasat with seismic-reflection and free-air gravity data by comparing selected profiles over the Fifteen-Twenty and the Tyro fracture zones in the central North Atlantic.

However, no quantitative study of the match between the topography and the geoid expression of a fracture zone in the Atlantic Ocean has been published yet. The central question is, how well are we able to map a fracture zone by picking the geoid troughs that seem to accompany the fracture zone valley? We know qualitatively that the geoid low usually follows the valley, but the short-wavelength topography of the ocean floor may not necessarily be the only variable reflected in the high-frequency geoid. Density anomalies in the crust, as described for example by Abrams *et al.* (1988) in the area of the eastern ridge-transform intersection of the Kane Fracture Zone, can overprint the basement topography in the geoid.

To better establish the relations between geoid and fracture-zone topography in slow-spreading crust, we have made a detailed comparison between 37 filtered geoid profiles from Geosat and the corresponding subsatellite profiles of depth to basement over the Kane Fracture Zone in the central North Atlantic.

The Kane Fracture Zone was chosen for this study because its location, topography and associated geophysical parameters are better known than those of any other fracture zone in the Atlantic Ocean. The morphology and crustal structure of the active transform and the transverse ridge of the Kane Fracture Zone were described in detail by Abrams *et al.* (1988) and Pockalny *et al.* (1988). Tucholke and Schouten (1988) mapped the basement structure of the Kane Fracture Zone over nearly its entire length from the East Coast Magnetic Anomaly off Cape Hatteras to the middle of the M-series magnetic anomalies west of Africa. This data set provides a unique opportunity to compare the morphology and structure of the fracture zone with Geosat altimetry data.

Data Base

The basement topography along subsatellite profiles was digitized from ten maps by Tucholke and Schouten (1988) that show structure contours on basement. These charts, contoured at a 250 m interval, are based on U.S. Navy bathymetric maps (narrow-beam and multibeam surveys), supplementary wide-beam echosounding, and seismic reflection profiles, which were used to correct the maps for

sediment cover. Digitizing errors for the subsatellite profiles are within $\pm 0.01^\circ$ (± 1 km) in distance.

Magnetic anomaly data for the central Atlantic used in this study (Figure 3) are from Klitgord and Schouten (1986). Assigned ages of magnetic anomalies are based on the time scale of Kent and Gradstein (1986).

We utilized unclassified Geosat altimetry data to determine the geoid and the deflection of the vertical across the Kane Fracture Zone. During its secondary mission, the satellite was placed in a 17-day repeat orbit with ground tracks spaced 164 km apart at the equator. The satellite altimeter measured the relative height of the sea surface to a precision of 3.5 cm for significant waveheights of 2 m (McConathy and Kilgus, 1987; MacArthur *et al.*, 1987). For our study, we used 37 descending Geosat tracks crossing the Kane Fracture Zone between 72° W and 24° W (Figure 2).

Isochron Chart of the Central North Atlantic

Minor modifications were made to the plate-kinematic model of Klitgord and Schouten (1986) in order better to match magnetic anomalies and fracture-zone lineations in the central Atlantic that were interpreted from combined magnetic and Geosat altimetry data (Figure 3). Plate reconstructions were made using interactive computer graphics to determine finite poles of rotation that best fit a pair of corresponding magnetic anomalies and fracture-zone lineations. The reconstruction poles for finite anomalies 5, 13, 21, 25 and 30 were slightly modified for improved fit of major fracture zone lineations (Table I).

Subsequently, stage poles were calculated for every stage (Table II) and reconstructions for all time slices, as listed in Table I, were plotted keeping North America fixed. These plots included superimposed magnetic anomaly picks for the reconstruction time as well as the older anomaly picks. Lineations in the deflection-of-the-vertical field and calculated small circles for the stage bounded by the next older anomaly pair were also plotted on the maps. Then continuous isochrons were drawn, connected by transforms. The paleo-ridge segments were drawn by finding the best average lines for superimposed magnetic picks. The positions of transforms between paleo-ridge segments were

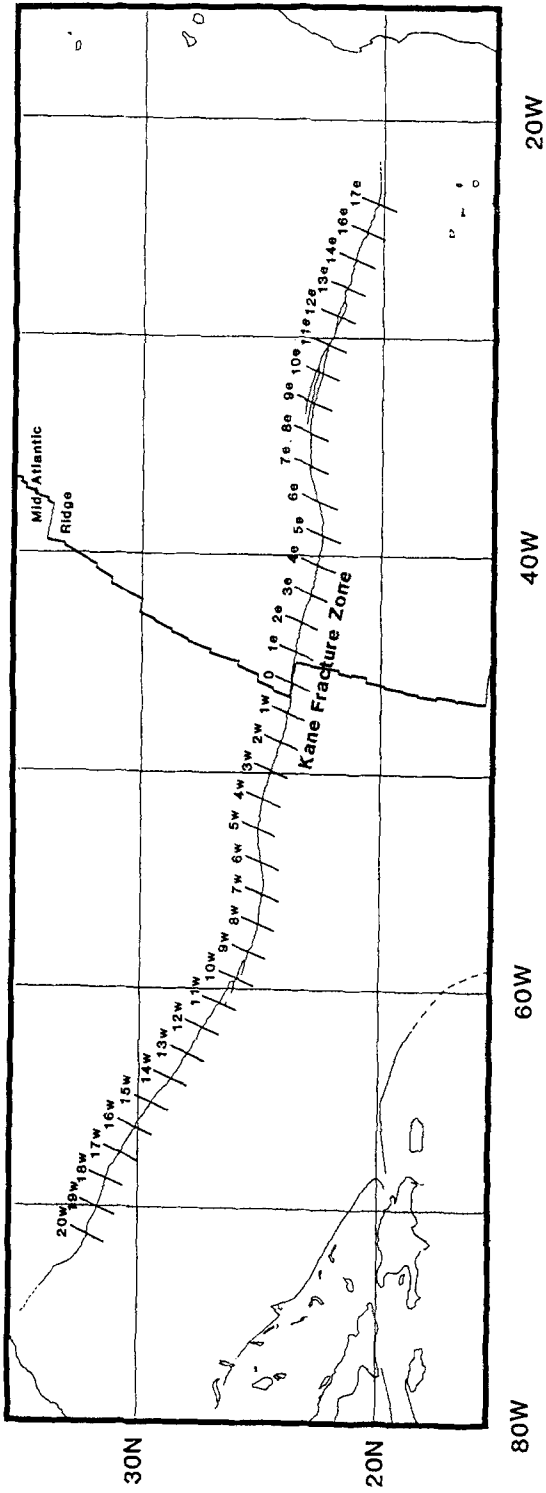


Fig. 2. Location of descending Geosat profiles used in this study. All profiles are 160 km long and are centered on the Kane Fracture Zone for which the trace of the axis of maximum depth is shown (from Tucholke and Schouten 1988).

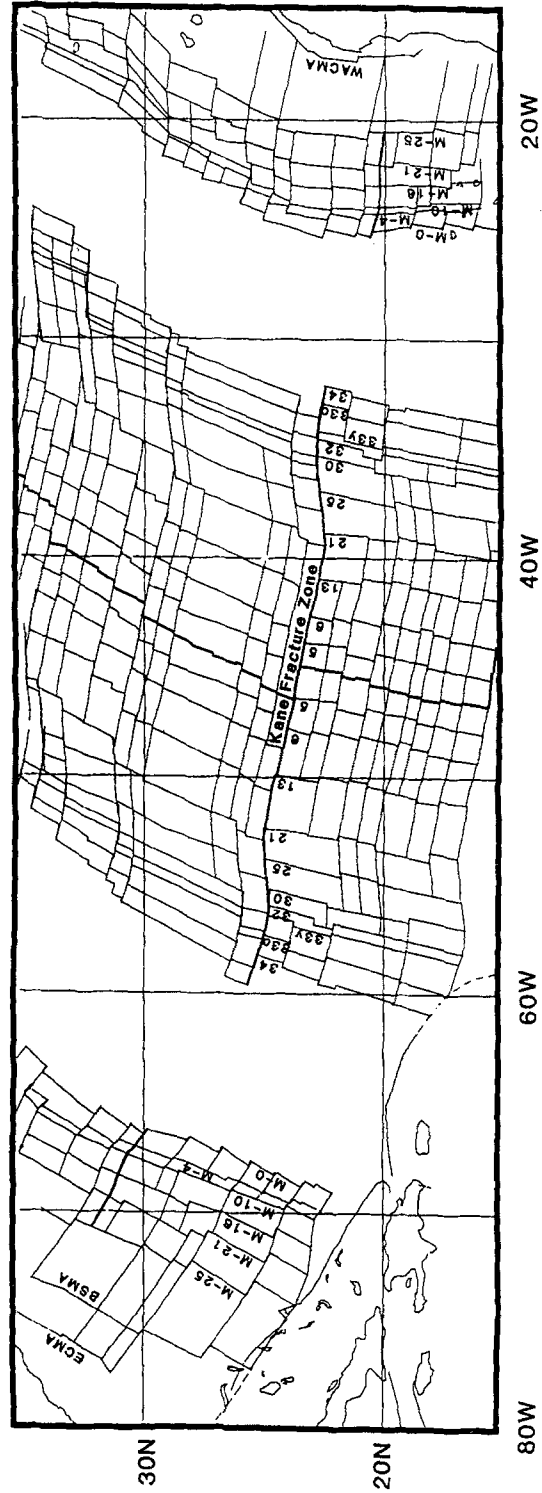


Fig. 3. Isochrons and synthetic plate flowlines of the ocean floor in the central North Atlantic based on a plate model slightly modified from Klitgord and Schouten (1986). (ECMA), East Coast Magnetic Anomaly; (BSMA), Blake Spur Magnetic Anomaly; (WACMA), West African Coast Magnetic Anomaly.

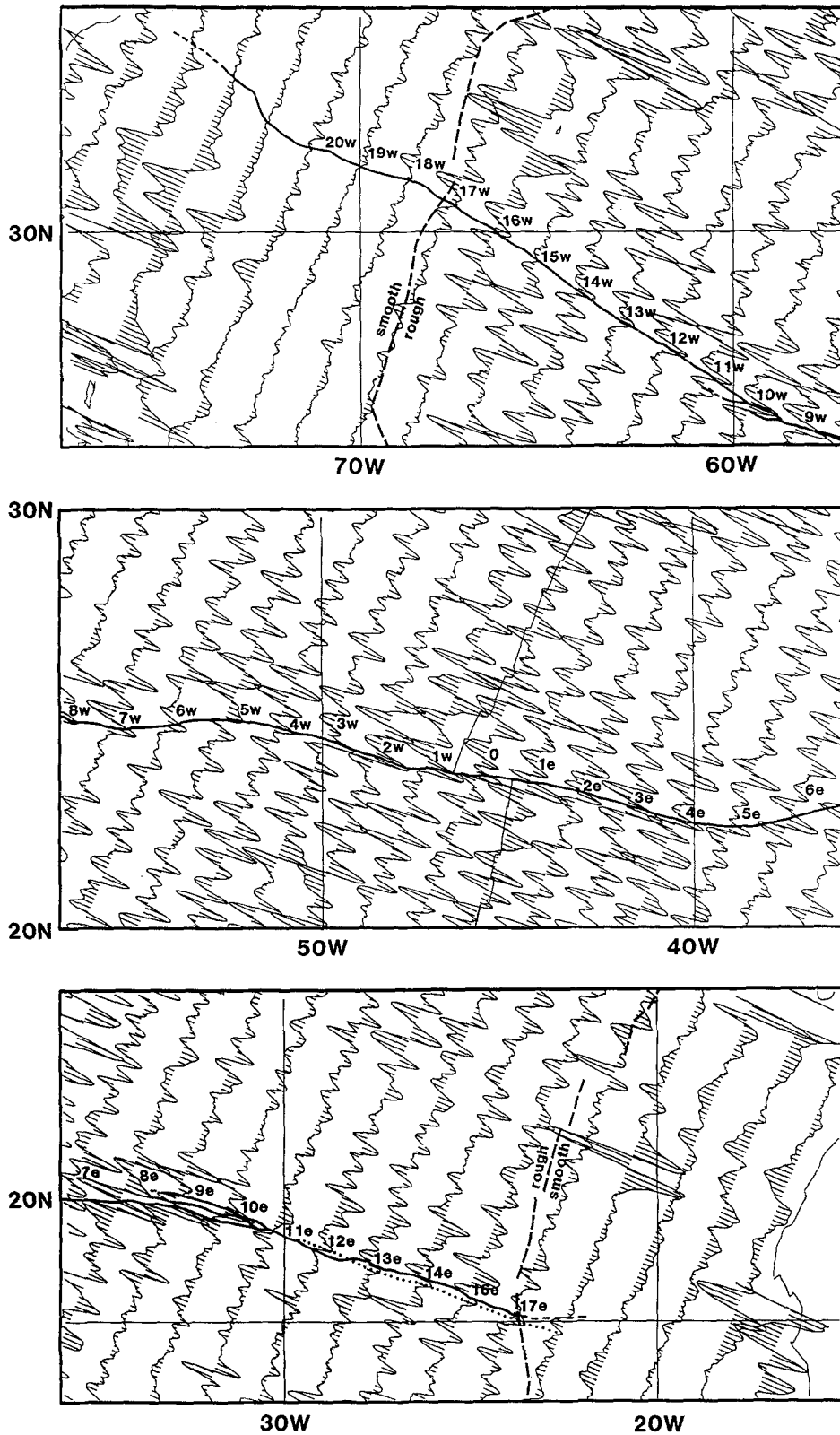


Fig. 4. Short-wavelength ($\lambda = 25-100$ km) geoid anomalies plotted along-track across the Kane Fracture Zone as identified by Tucholke and Schouten (1988) from basement structure. The geoid in Figures 4a and 4c is plotted at a scale of 10 cm deg^{-1} , in Figure 4b at a scale of 15 cm deg^{-1} . The boundary between rough and smooth basement (from Sundvik *et al.* (1984)) is indicated, and it correlates well with a change in amplitudes of the geoid signal.

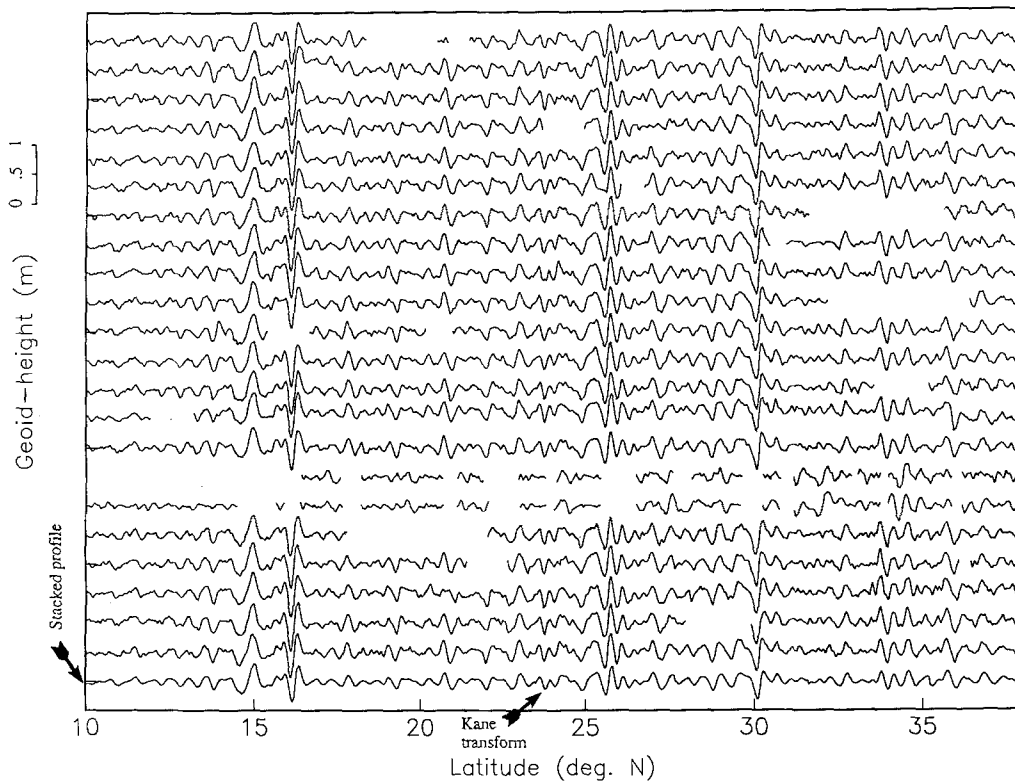


Fig. 5. To determine the noise level in the stacked, filtered geoid profiles, we averaged 22 repeat cycles together that cross the active transform of the Kane Fracture Zone. This was done by first integrating the slopes of individual profiles and then high-pass filtering the geoid data. After averaging the data together, the mean, standard deviation (σ), and the error in the mean (σ/\sqrt{N}) (N = number of repeat cycles) were determined (see Figure 5).

determined by offsets in magnetic lineations and by deflection-of-the-vertical lineations, which provide additional constraints for the location of fracture zones, especially where magnetic data are sparse.

The fracture-zone segments for different stages were drawn as synthetic flowlines, which are defined by small circles about the stage poles. This procedure yielded isochrons for the plate that was kept fixed in the reconstructions (i.e. North America). A complete set of isochrons (Figure 3) was derived by rotation of every isochron from the North American plate to its corresponding position on the African plate, using the finite reconstruction poles in Table I with the angle of opening reversed. We used this isochron map to determine the approximate paleo-offsets in kilometers along the Kane Fracture Zone.

Data Analysis

The Geosat data used in this study were edited and compressed from 10 points per second to 2 points per second as described in Sandwell and McAdoo

(1988). This resulted in an along-track distance of 3.33 km between data points. The along-track Geosat resolution is about 30 km (Sandwell and McAdoo, 1990), 20 km better than Seasat data that reached a resolution of 50 km (Marks and Sailor, 1986). In order to suppress the high-frequency noise in the geoid data, stacking of repeat tracks is necessary. The geoid data cannot be stacked easily, though, because Geosat repeat cycles have unknown long-wavelength biases of 1–2 m and contain data gaps. Such data gaps can be caused by the gravity-gradient stabilization system of the satellite that is not always able to maintain the nadir direction to within a 1° tolerance (Sandwell and McAdoo, 1988). As a consequence, the altimeter occasionally does not regain its lock after moving from land to sea. Data gaps are also caused by editing the Geosat data as mentioned above. The combined effects of the long-wavelength bias and data gaps in individual repeat profiles produce steps in the average profile if the geoid data are stacked. To remove the unknown bias, we take the derivative of the individual profiles

TABLE I
Reconstruction poles for the African plate relative to the North American plate

Anomaly no.	Age (Ma)	Latitude	Longitude	Angle	Source
5	10.0	80.12	50.80	2.52	Müller <i>et al.</i> (1990, this paper)
6	20.0	79.57	37.84	- 5.29	Klitgord and Schouten (1986)
13	35.5	75.37	1.12	-10.04	Müller <i>et al.</i> , (1990, this paper)
21	49.5	75.30	- 3.88	-15.25	Müller <i>et al.</i> , (1990, this paper)
25	59.0	79.68	- 0.46	-18.16	Müller <i>et al.</i> , (1990, this paper)
30	67.5	82.90	4.94	-20.76	Müller <i>et al.</i> , (1990, this paper)
32	72.5	81.35	- 9.15	-22.87	Klitgord and Schouten (1986)
33	74.3	80.76	-11.76	-23.91	Klitgord and Schouten (1986)
33	80.2	78.30	-18.35	-27.06	Klitgord and Schouten (1986)
34	84.0	76.55	-20.73	-29.60	Klitgord and Schouten (1986)
M-0	118.0	66.30	-19.90	-54.25	Klitgord and Schouten (1986)
M-4	126.0	66.13	-19.00	-56.39	Klitgord and Schouten (1986)
M-10N	131.5	65.95	-18.50	-57.40	Klitgord and Schouten (1986)
M-16	141.5	66.10	-18.40	-59.79	Klitgord and Schouten (1986)
M-21	149.5	66.50	-18.10	-61.92	Klitgord and Schouten (1986)
M-25	156.5	67.15	-16.00	-64.70	Klitgord and Schouten (1986)

TABLE II
Stage poles of motion

Anom. 1	Anom. 2	Latitude	Longitude	Angle
0	5	80.1	50.8	2.52
5	6	78.7	27.3	-2.77
6	13	68.0	-18.7	-4.88
13	21	75.2	-13.5	-5.22
21	25	77.4	143.2	-3.18
25	30	74.3	146.2	-2.83
30	32	61.6	-51.3	-2.31
32	33	67.3	-40.7	-1.08
33y	33o	60.2	-41.9	-3.37
33o	34	59.2	-38.8	-2.69
34	M-0	55.3	-29.0	-25.63
M-0	M-4	57.8	- 8.2	-2.17
M-4	M-10N	52.2	-10.8	-1.04
M-10N	M-16	68.4	-11.5	-2.40
M-16	M-21	72.0	9.4	-2.17
M-21	M-25	60.6	31.2	-2.99

Stage poles for the North American plate				
Anom. 1	Anom. 2	Latitude	Longitude	Angle
0	5	80.1	50.8	2.52
5	0	78.7	27.3	2.77
6	13	68.0	-18.7	4.88
13	21	75.2	-13.5	5.22
21	25	77.4	143.2	3.18
25	30	74.3	146.2	2.83
30	32	61.6	-51.3	2.31
32	33y	67.3	-40.7	1.08
33o	33	60.2	-41.9	3.37
33o	34	59.2	-38.8	2.69
34	M-0	55.3	-29.0	25.63
M-0	M-4	57.8	- 8.2	2.17
M-4	M-10N	52.2	-10.8	1.04
M-10N	M-16	68.4	-11.5	2.40
M-16	M-21	72.0	9.4	2.17
M-21	M-25	60.6	31.2	2.99

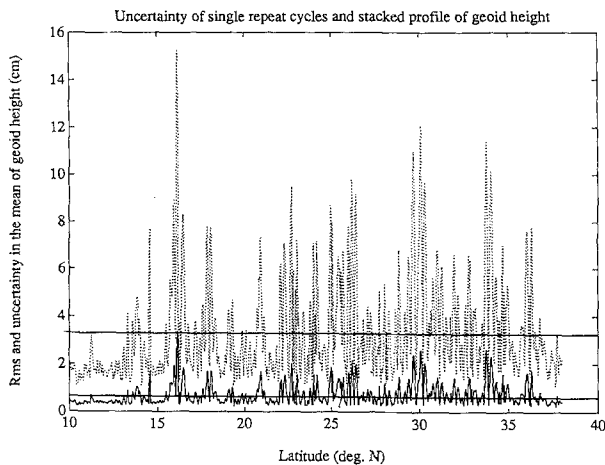


Fig. 6. Uncertainty in the geoid height ($\lambda = 25\text{--}100$ km). The average noise level is 3.3 cm for single repeat cycles (dotted line) and 0.7 cm for stacked profile (continuous line).

before averaging them together. We then integrate the average slope profiles to reconstruct the geoid height with an unknown bias. If the Geosat profiles had no data gaps or inaccurate data, similar results could be obtained by a simpler processing procedure such as (1) band-pass filtering individual profiles, (2) resampling, and (3) stacking of the profiles. However, editing of Geosat data with insufficient accuracy eliminates about 16% of the data (Sandwell and McAdoo, 1990). The editing must be done before filtering the data, since the resulting irregular data gaps would cause edge effects after band-pass filtering the data. In this case even more data would have to be eliminated and the size of the data gaps would increase. For this reason we first apply a derivative filter after editing the data, since its edge effect amounts to only one percent. Another reason for our more complicated processing procedure is to obtain a stacked Geosat data set that is not high-pass filtered so that it can be used for other studies as well. All operations involved in our processing technique are linear, except for the editing, so that the order in which they are applied is irrelevant. The details of the processing follow.

As the first step in the data processing, the time derivative of each set of repeat cycles was formed. This derivative enhances the short-wavelength portion of the signal and suppresses the longer-wavelength radial orbit error and the path-length errors (Sandwell and McAdoo, 1988). To suppress short-wavelength noise that is amplified by the first deriva-

tive, the data were convolved with a Gaussian filter ($\exp[-t^2/2\sigma^2]$, $\sigma = 0.7$ s), corresponding to a half-power point of 25 km wavelength. The filtered slope profile was then resampled on a uniform along-track spacing. Together with the derivative filter, we obtained a half-power point wavelength of 14 km for the resulting low-pass filter. Next, the stacked time derivative was obtained by averaging 22 repeat cycles to obtain complete coverage and to decrease the short-wavelength noise.

In order to obtain the stacked along-track geoid, we integrated the time-derivative. We then computed the mean difference between the geoid height and the PGS-S4 gravity model (Marsh and Martin, 1982), and subtracted the resulting constant from each geoid track. To decrease the long wavelengths in the geoid, we applied a Gaussian high-pass filter with $\sigma = 2.8$ s ($\lambda = 100$ km). Spectral analyses of bathymetry and free-air gravity data along ship tracks in the central and South Atlantic (McKenzie and Bowin, 1976), as well as over the Kane Fracture Zone (Louden and Forsyth, 1982) indicate that long-wavelength topography ($\lambda > 100$ km) is isostatically compensated and shorter wavelength topography is uncompensated. Louden and Forsyth (1982), explained their observations using a model requiring regional isostatic compensation and short-wavelength topographic anomalies that are supported by an elastic plate of about 6 km thickness. Twigt *et al.* (1983) compared topography, free-air gravity and computed free-air gravity anomalies for three profiles across the eastern limb of the Kane Fracture Zone in the Cretaceous magnetic quiet zone. They found the best fit for a model of regional isostatic compensation for wavelengths longer than 100 km, an oceanic crustal thickness of 5 km, and a crust-mantle interface that follows oceanic basement topography. These studies suggest that a wavelength of about 100 km marks the transition from isostatically uncompensated to compensated ocean crust along the Kane Fracture Zone. Because geoid anomalies with wavelengths longer than 100 km are largely unrelated to basement topography, we chose a high-pass filter that eliminates those wavelengths. Figure 4 shows the resulting stacked, filtered geoid data ($\lambda = 25\text{--}100$ km) plotted along descending Geosat tracks.

In order to determine the noise level in the filtered geoid profiles we chose a set of 22 repeat cycles that

cross the active transform of the Kane Fracture Zone (Figure 5), integrated the slopes of individual profiles, and high-pass filtered the geoid data as described above. We then averaged the profiles together and determined the mean, standard deviation (σ), and the error in the mean (σ/\sqrt{N}) (N = number of repeat cycles). The average noise level, 3.3 cm for single repeat cycles, is reduced to 7 mm for the stacked profile (Figure 6).

For the analyses presented in this paper, descending Geosat tracks of 160 km length crossing the Kane Fracture Zone (Figure 6) were selected. Both the subsatellite profiles of basement depth and the geoid profiles were projected perpendicular to the fracture valley to eliminate the effect of angle of incidence on wavelength of the geoid signal.

Figure 7 shows the ratio between geoid height and basement topography for the eastern and western limbs of the Kane Fracture Zone. The ratio was obtained by calculating the zero-phaseshift cross-correlation value between geoid and basement depth. In the frequency domain this corresponds to calculating the admittance but using only the real part of the cross-spectrum. This implies that the cross-correlation is symmetric. A commonly used procedure is to extract the symmetric part of the cross-correlation function, which is assumed to be highest at zero lag. Calculating the zero-lag cross-correlation in the time-domain directly corresponds to this procedure.

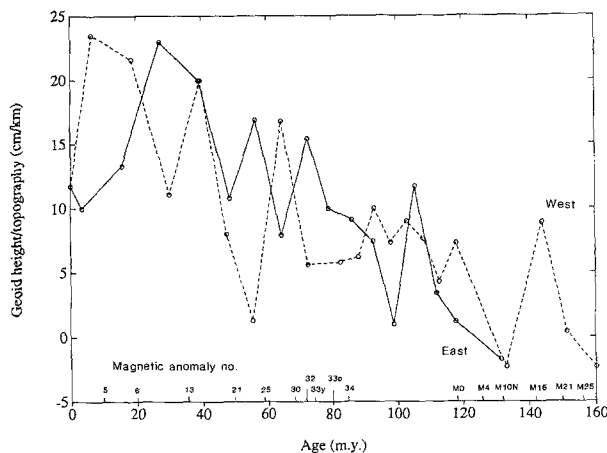


Fig. 7. Geoid height/topography ratio for the eastern (continuous line) and western (dashed lines) limbs of the Kane Fracture Zone determined for zero phase lag in the cross correlations shown in Figures 10–19.

In order to evaluate quantitatively the correlation between the basement topography and the short-wavelength geoid signal of the Kane Fracture Zone, we determine the phase lag between the two signals by cross correlation (Figure 8) as well as by visual comparison (Figure 9). Cubic-spline interpolation was used to resample both signals with equal intervals of 3 km, and the mean of both data sets was reduced to zero. In order to emphasize the cross correlation of the central parts of the profiles, namely troughs in the geoid and basement topography, we applied a hanning window (Press *et al.*, 1986) to all profiles. The cross correlations were normalized by dividing the results by the variance or total energy of the basement topography (i.e. the lag-zero autocorrelation value of the basement topography). This yields the geoid-height/topography ratio as a function of horizontal offset between geoid height and topography (Figures 10–19).

The cross correlations (Figures 10–19) show that for all profiles on ocean crust younger than 130–140 Ma there is generally a good (peaked) correlation. Profiles on older ocean crust (Figures 10, 19), however, show a relatively poor (broad) correlation.

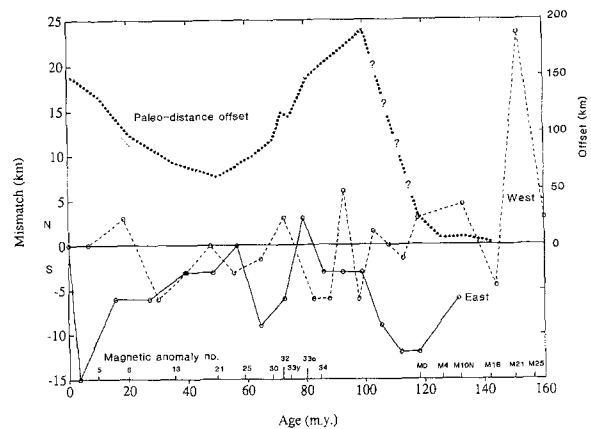


Fig. 8. Phase lag between the central fracture-zone troughs in the geoid and the depth to basement for the eastern (continuous lines) and western (dashed lines) limbs of the Kane Fracture Zone as determined by cross correlation. Although the cross correlation provides an objective statistical method to determine the correlation between geoid height and topography, it may over- or underestimate the actual offset between geoid trough and fracture-zone valley. This is caused by topographic features such as ridges in the vicinity of the trough that affect the cross correlation, so that the result is not purely based on the mismatch of the two troughs. The mean phase lag between geoid height and topography is 5.5 km.

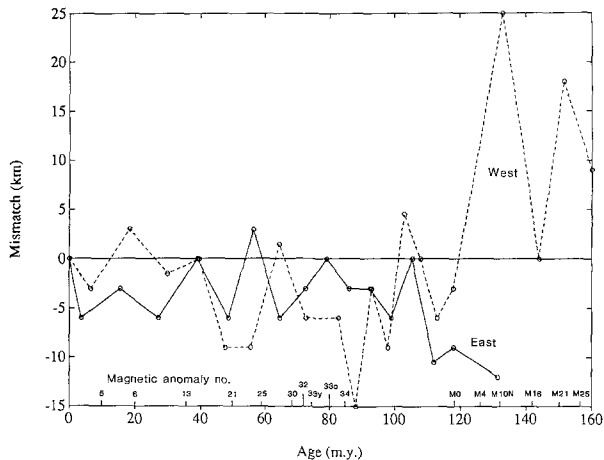


Fig. 9. Phase lag between the central fracture-zone troughs in the geoid and the depth to basement for the eastern (continuous lines) and western (dashed lines) eastern (continuous lines) limbs of the Kane Fracture Zone as determined by visual correlation. The mean phase lag between troughs in the geoid and topography determined by visual comparison is 4.3 km, very close to the 5.5 km value determined by cross-correlation. The average paleo-offset of the Mid-Atlantic Ridge axis at the Kane transform is displayed as a dotted line. The phase lags between geoid and topography show no correlation with paleo-offset.

For the younger profiles the average phase lag between geoid height and topography is 5.5 km (Figure 8).

A closer look at the results of the cross correlations of individual profiles shows that although the correlation was weighted towards the center parts of the profiles, the results of the cross correlation sometimes do not give the actual offset between geoid trough and topography trough. Since topographic features in the vicinity of the valley, like pronounced ridges, do have a significant effect on the cross correlation, the results are not based purely on the mismatch of the two troughs. Hence, in addition we have done a visual comparison of the match between the troughs in the geoid and the topography, which resulted in a mean mismatch of 5.0 km, compared to the mean mismatch of 5.5 km derived by the cross

correlation. For most of the profiles, both methods yield very similar results. The cross correlation method, (Figure 9) however, sometimes under- or overestimates the actual mismatch, depending on the trough-parallel topography. A good example is profile 1e that crosses the transverse ridge just east of the Kane transform (Figures 2, 15). Here the cross correlation puts emphasis on the match between the positive peaks of the geoid height and the topography over the transverse ridge, resulting in a seemingly good correlation, although the geoid trough is offset by about 15 km from the fracture valley.

Interpretation

The ratio between geoid height and basement topography averages about 10 cm/km in the Kane Fracture Zone crossings studied (Figure 7), but there is a clear trend toward decreasing geoid signal with increasing age of the ocean crust. This trend reflects increasing basement depth with increasing age out to ca. 60–70 m.y. Crustal depths at greater ages, however, remain relatively constant or even shoal, as over the Bermuda Rise in the western basin (Figure 20). At these ages, therefore, the decreased geoid height/basement-topography ratio must be caused by other factors. One prominent effect is sediment infill of the fracture valley; the infill attenuates the geoid signal and becomes increasingly important over older crust (Tucholke *et al.*, 1982; Figure 20). A second contributing factor is decreased overall basement relief of the fracture valley. The reduced relief relates to small offset of the contemporaneous transform in old crust (Figure 9) as well as effects of plate-motion change (e.g. sheared crust on east flank, Figure 20).

The geoid-height/basement topography ratio in Figure 7 also shows large variability with distance (age) along the fracture valley. The variability is

Figs. 10–19. Cross correlations between geoid height and basement topography of 37 profiles that cross the Kane Fracture Zone. Left: Basement topography (dotted) and geoid height (solid). Right: Resulting cross correlations. All profiles are viewed as if looking west along fracture zone. Ages noted on each panel are for the crust on the young side of the fracture zone. All profiles are projected perpendicular to the Kane Fracture Zone valley. Both geoid and basement depth signals were resampled at equal intervals of 3 km, and their mean was reduced to zero. Profiles 1w to 20w are on the North American Plate, profiles 1e to 17e on the African plate, and profile 0 crosses the active transform of the Kane Fracture Zone. Profiles were numbered so that profiles with the same number (e.g. 10w, 10e) cross oceanic crust of about the same age. This allows ready comparison of corresponding profiles from the North American and African plates. Profile number 15e is omitted, because the age difference of the ocean floor between the equally spaced profiles is not symmetric between the North American and African plates.

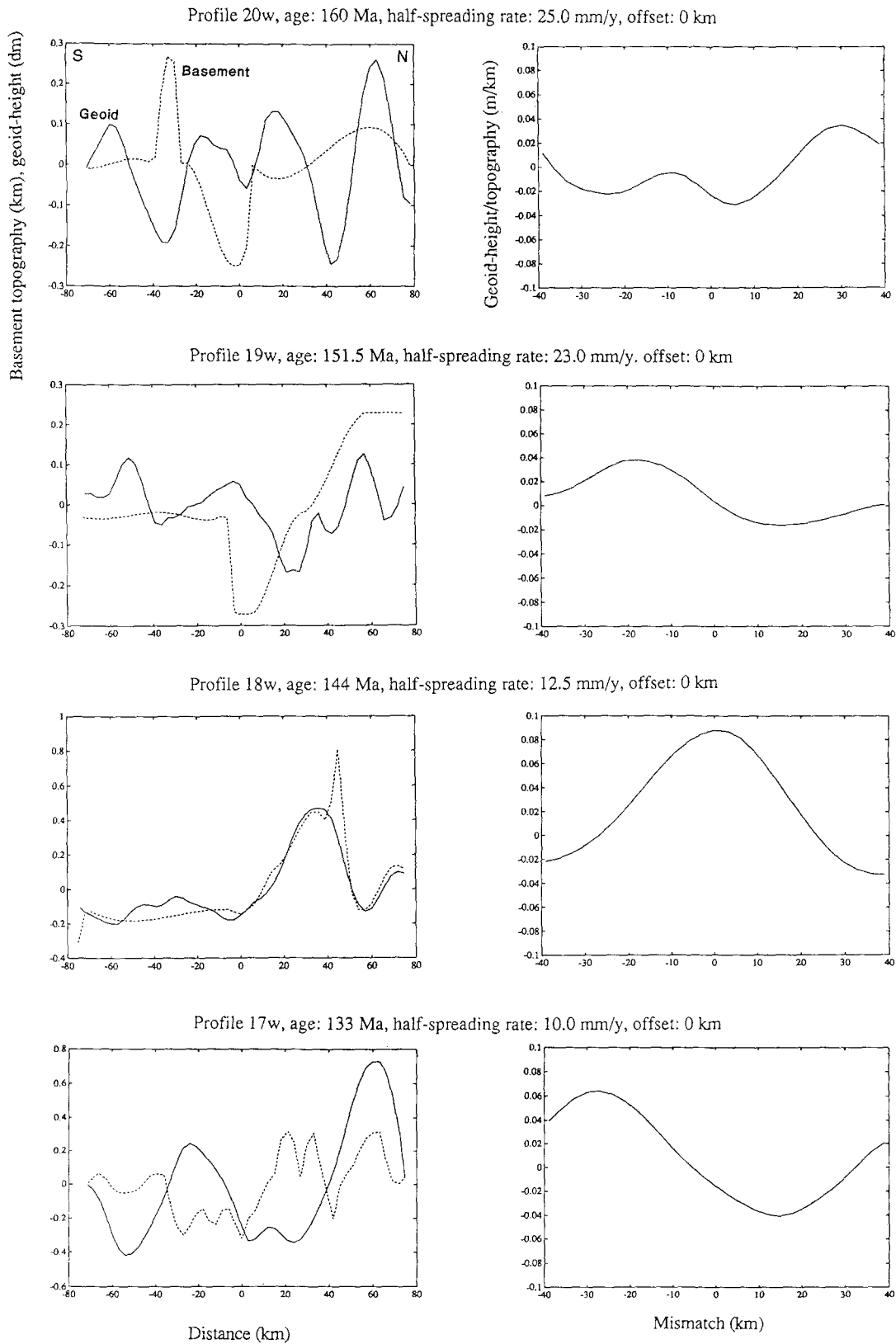


Fig. 10. Profiles 20w to 17w (age of crust: 160–133 Ma). The poor correlation between geoid and basement depth for profiles 20w to 17w primarily reflects poor control on basement depth in this area.

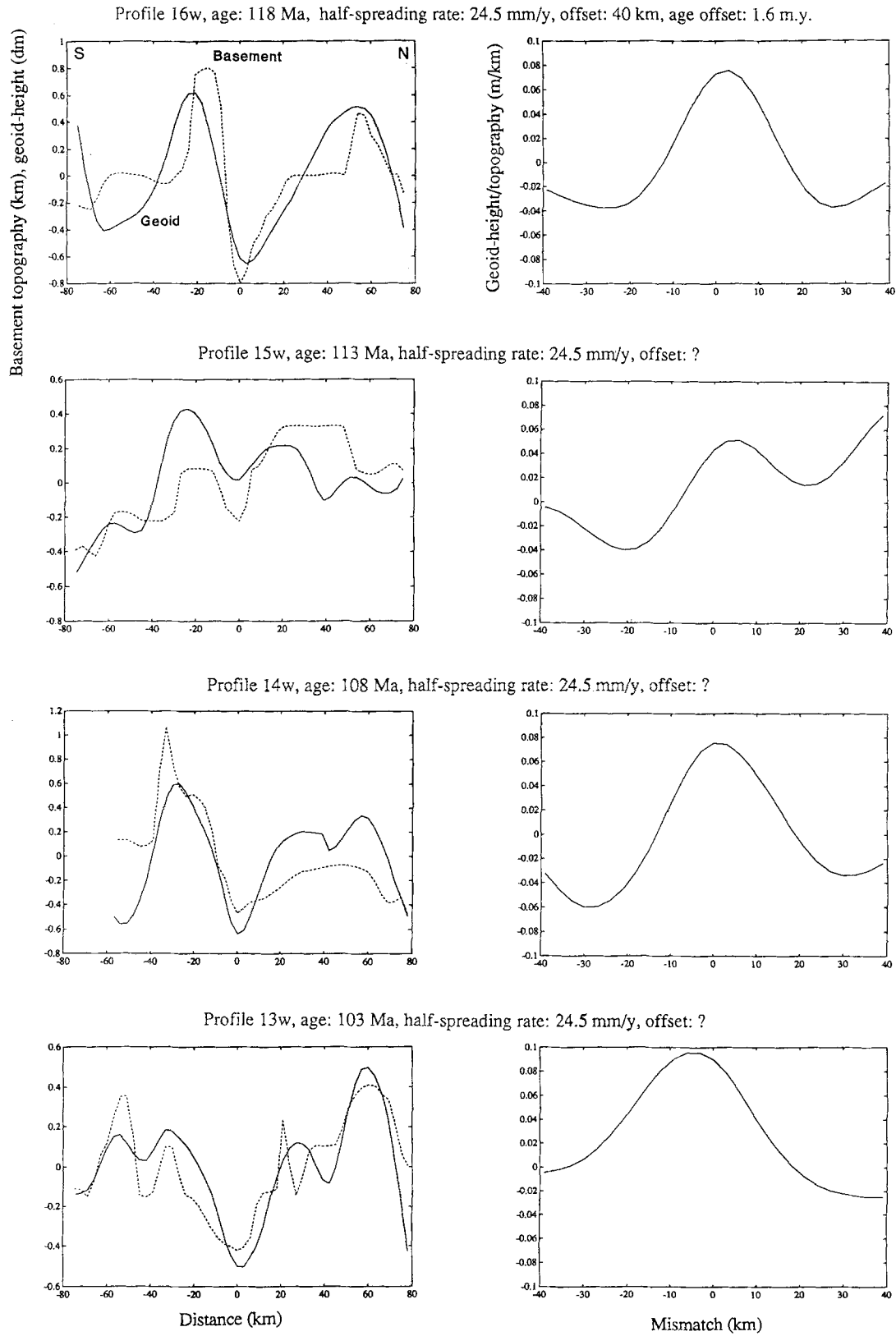


Fig. 11. Profiles 16w to 13w (age of crust: 118–103 Ma).

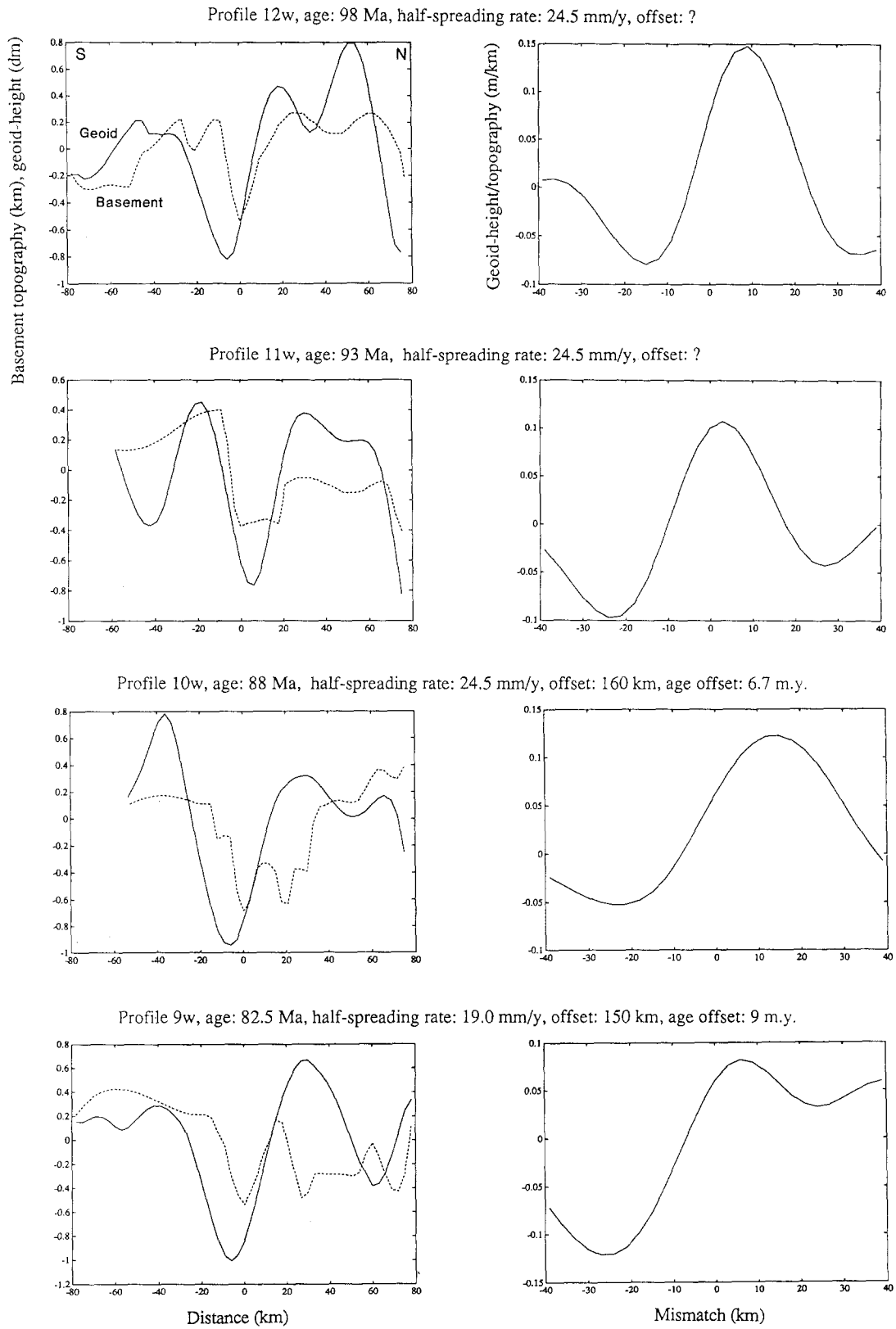


Fig. 12. Profiles 12w to 9w (age of crust: 98–82.5 Ma).

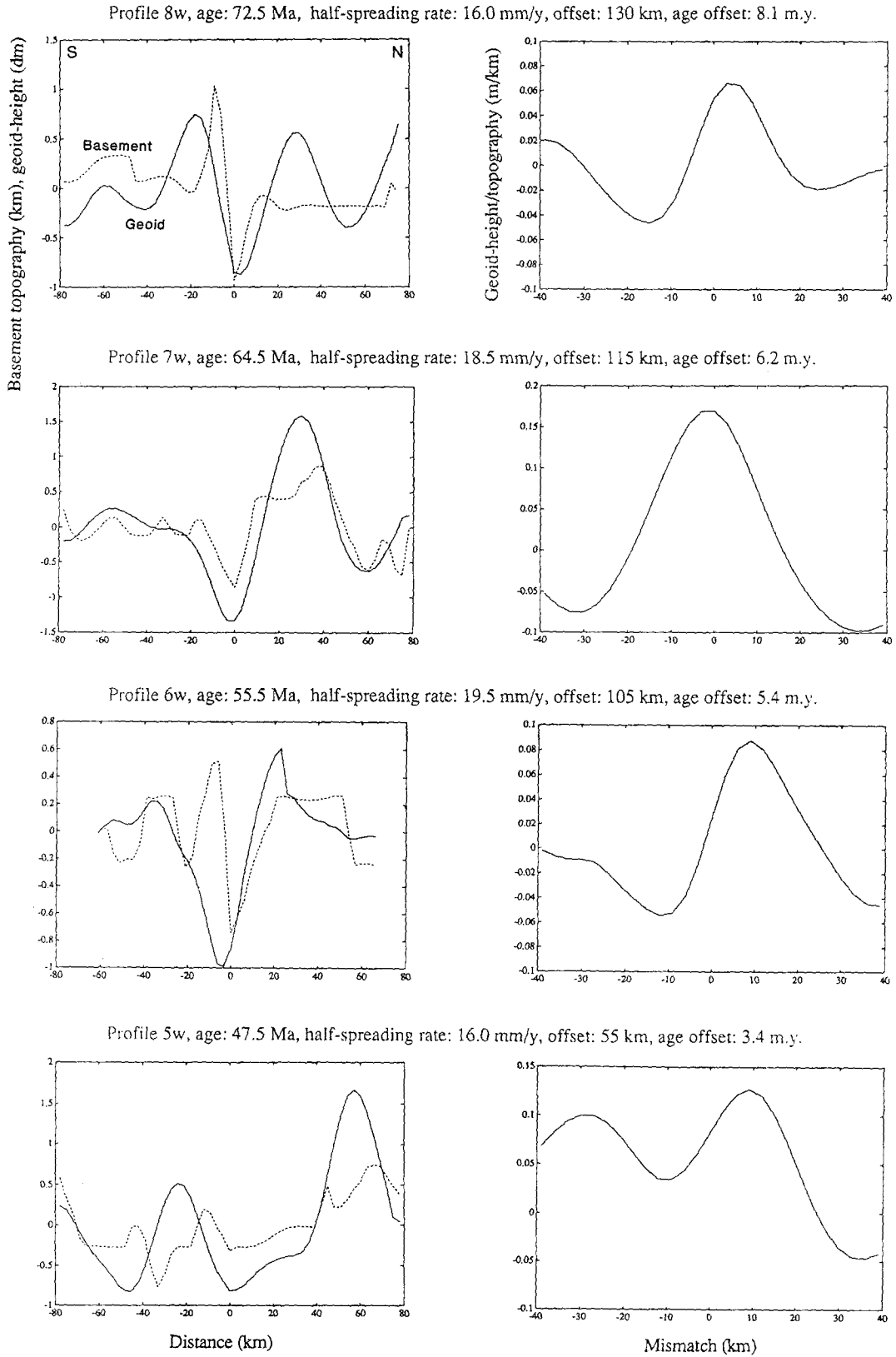
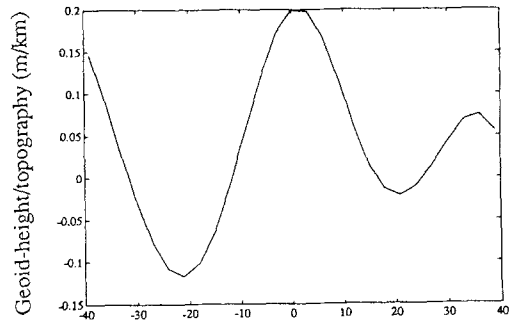
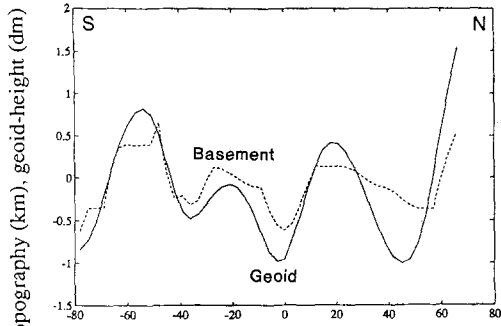
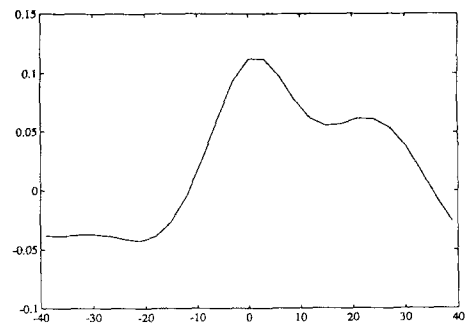
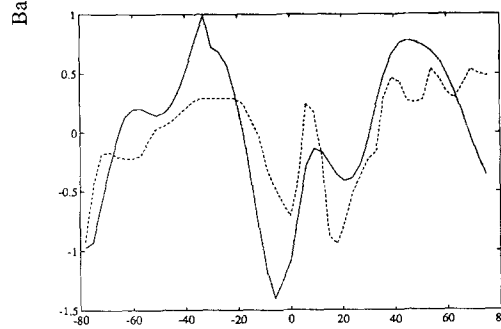


Fig. 13. Profiles 8w to 5w (age of crust: 72.5–47.5 Ma).

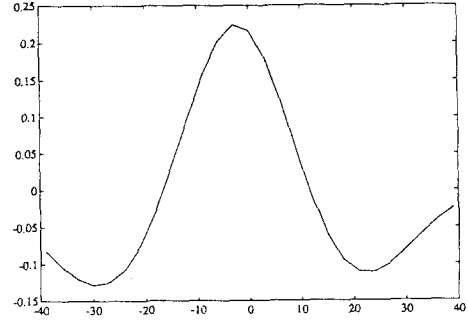
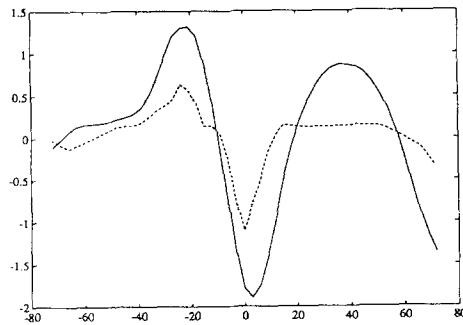
Profile 4w, age: 39.5 Ma, half-spreading rate: 16.0 mm/y, offset: 85 km, age offset: 5.3 m.y.



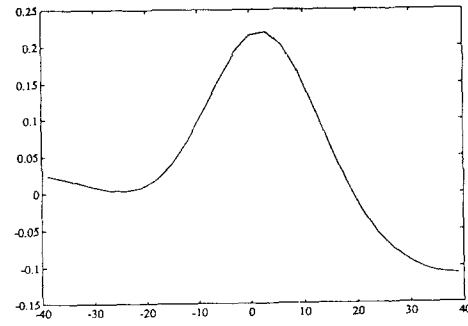
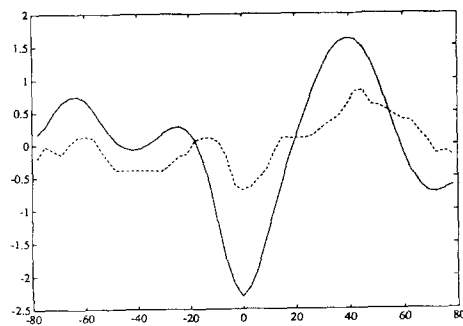
Profile 3w, age: 30 Ma, half-spreading rate: 13.0 mm/y, offset: 85 km, age offset: 6.5 m.y.



Profile 2w, age: 18.5 Ma, half-spreading rate: 14.0 mm/y, offset: 105 km, age offset: 7.5 m.y.



Profile 1w, age: 6.5 Ma, half-spreading rate: 12.0 mm/y, offset: 150 km, age offset: 12.5 m.y.



Distance (km)

Mismatch (km)

Fig. 14. Profiles 4w to 1w (age of crust: 39.5–6.5 Ma).

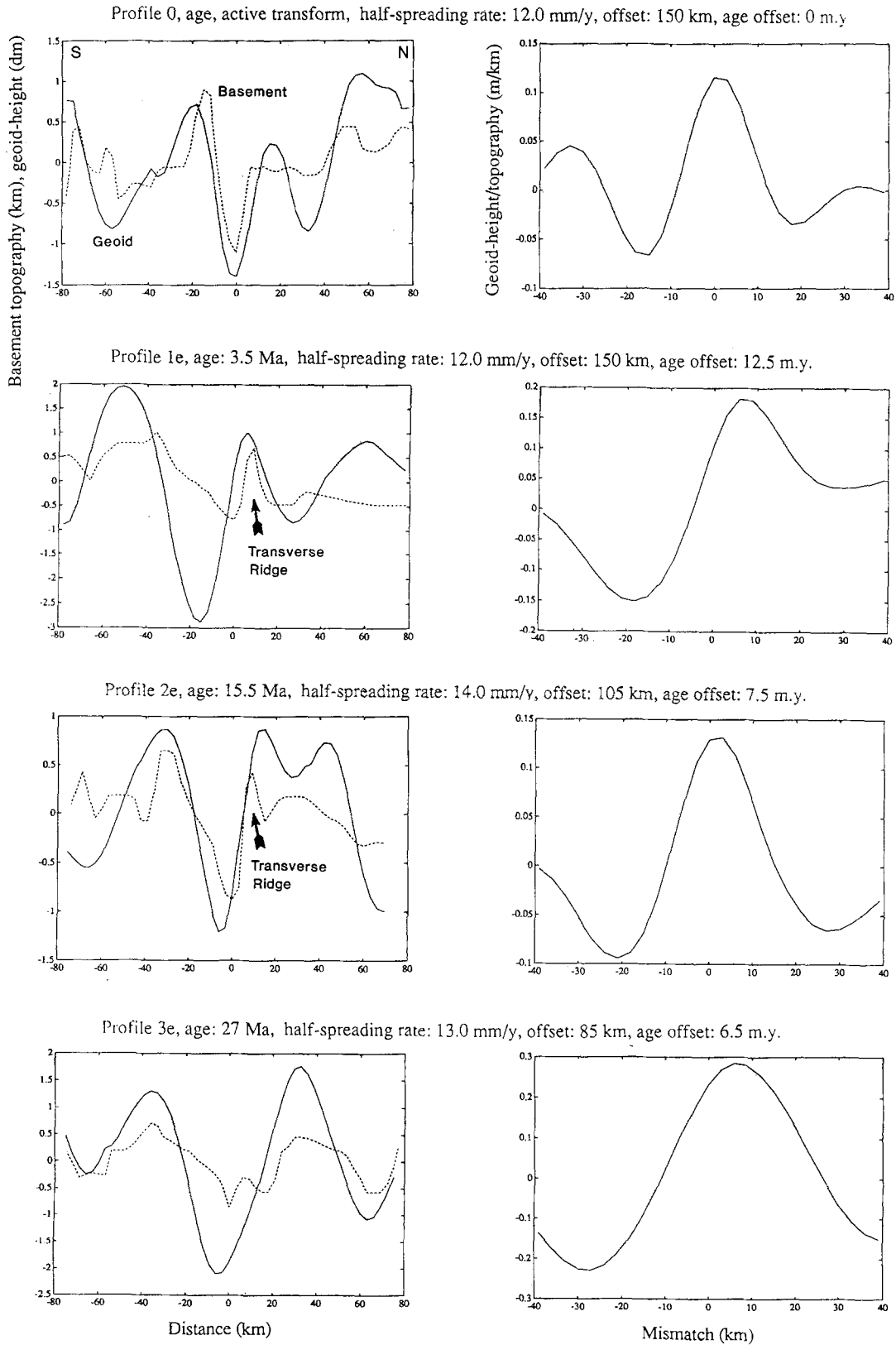


Fig. 15. Profiles 0 to 3e (age of crust: 3.5–27 Ma). A distinct phase shift (~ 15 km) between geoid and basement depth occurs directly east of the active transform of the Kane Fracture Zone, where a transverse ridge borders the northern edge of the fracture zone valley (profile 1e). This observed phase shift is consistent with a phase offset of 15–20 km between gravity and bathymetry in the same area. Abrams *et al.* (1988) explained the offset by a 20–30 km wide upwarp of the Moho beneath the isostatically uncompensated transverse ridge and the fracture-zone valley.

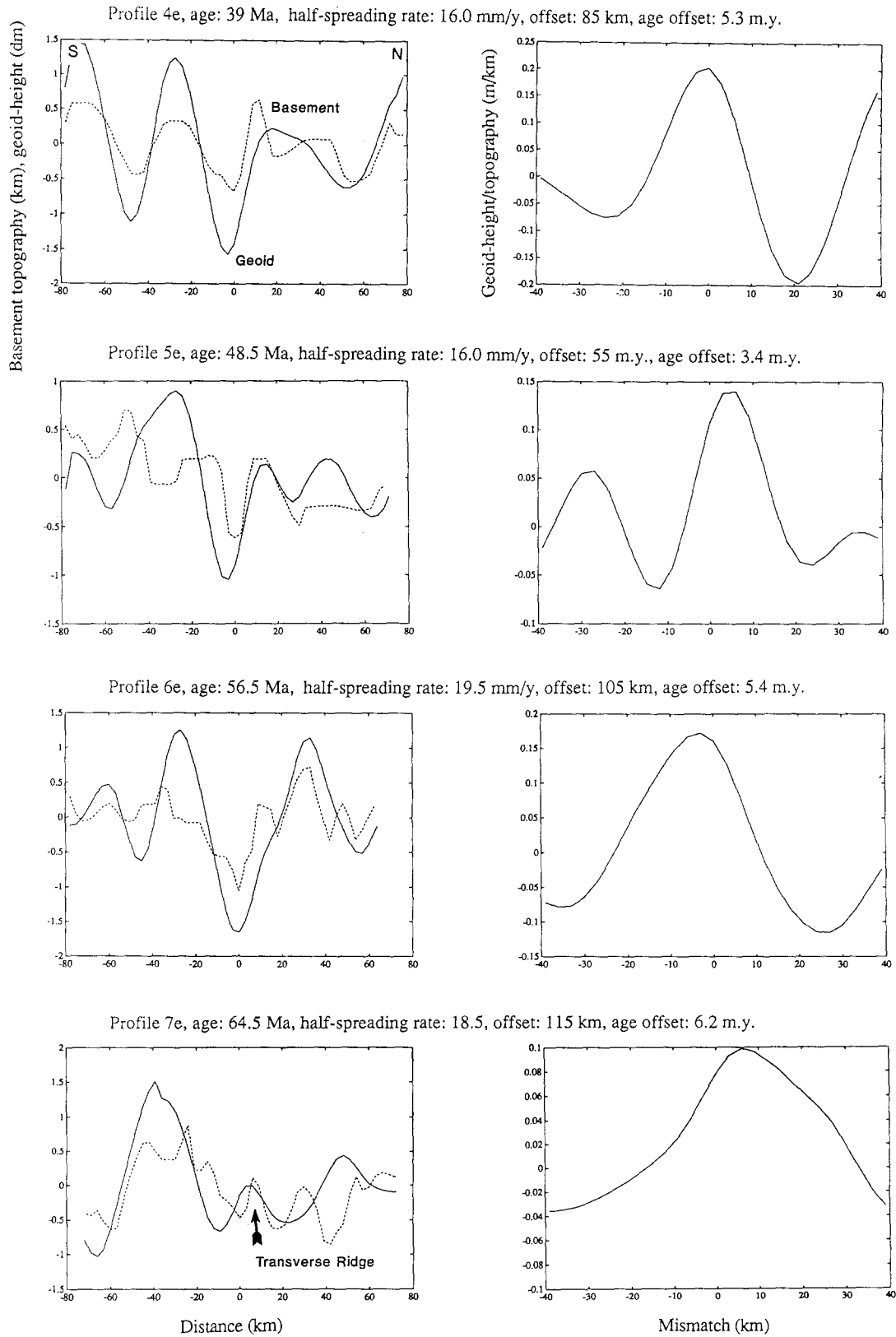


Fig. 16. Profiles 4e to 7e (age of crust: 39–64.5 Ma).

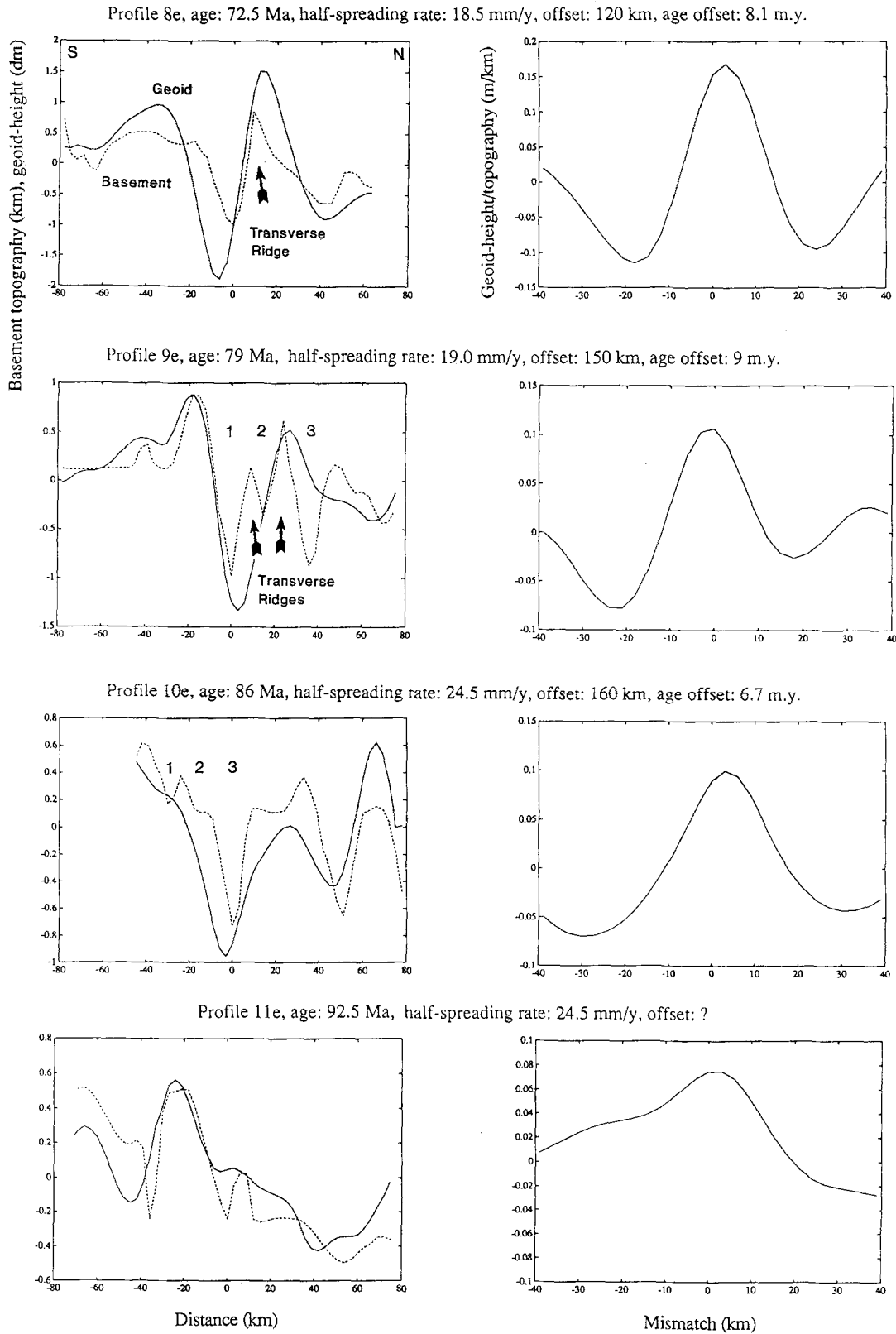


Fig. 17. Profiles 8e to 11e (age of crust: 72.5–92 Ma). Profile 9e crosses an area where three parallel fracture-zone segments (1, 2, 3) formed during a counterclockwise change in spreading direction that started in the Cretaceous Quiet Zone (Tucholke and Schouten, 1988). The northern two fracture valleys merge in profile 10e. The geoid signal of profile 9e correlates well with the southernmost fracture valley. The northernmost valley, which has a topographic expression similar to the southern valley shows little geoid signature.

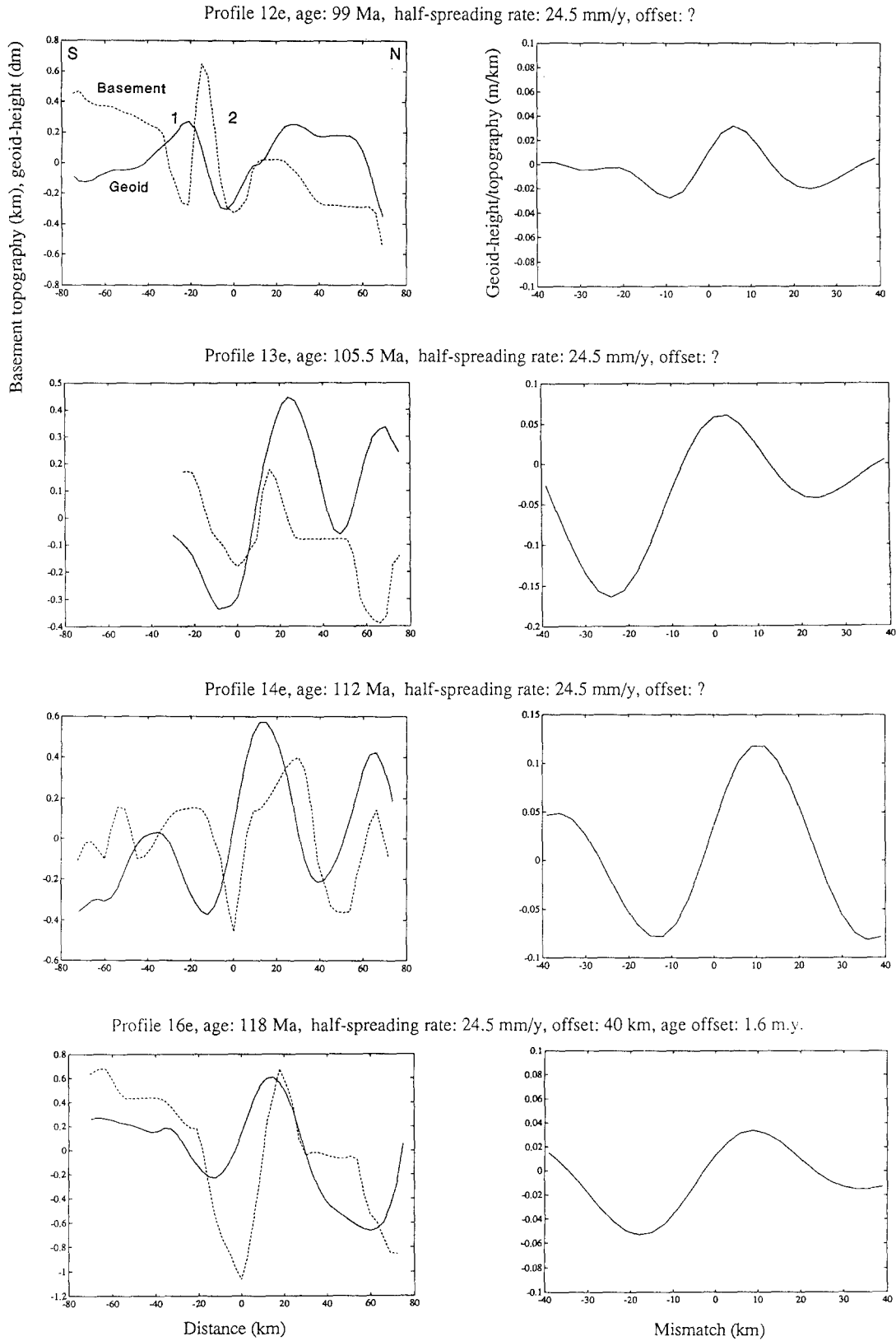


Fig. 18. Profiles 12e to 16e (age of crust: 98–118 Ma). In profile 12e the Kane Fracture Zone exhibits a northern and southern trough (1 and 2), created by a rapid clockwise shift in plate motion about 100–102 Ma (Tucholke and Schouten, 1988). The geoid trough is restricted to the northern fracture valley. See text for discussion.

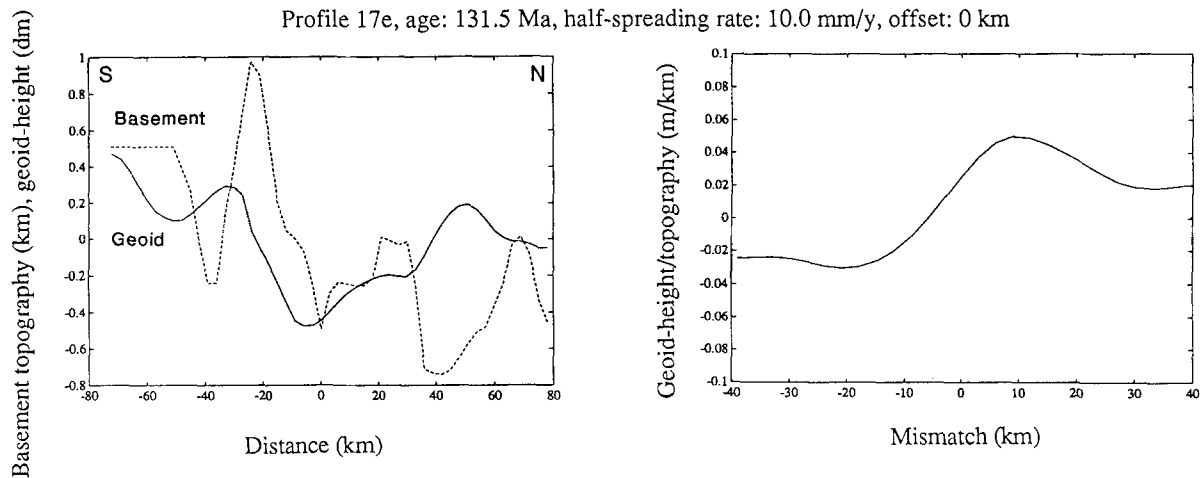


Fig. 19. Profiles 17e (age of crust: 131.5 Ma). The northernmost 60 km of the basement profile 17e are projected from basement contours about 4 km west of the geoid profile. This explains the poor fit between basement and geoid north of the fracture zone.

mainly caused by out of plane topography on the geoid signal (like large-amplitude basement highs and lows that commonly are close ($<5-10$ km) to the subsatellite tracks), the effect of sediment infill, and changes in crustal and upper mantle density and structure along the fracture valley.

Crustal thickness beneath fracture-zone troughs is variable but often is anomalously thin (2–3 km) (Detrick *et al.*, 1982; White *et al.*, 1984). Two, apparently different types of thinned fracture-zone crust have been recognized to date. The first is somewhat thinner (4–5 km) than normal oceanic crust and has lower seismic velocities. It has been identified at large-offset fracture zones such as Vema and Oceanographer (Sinha and Loudon, 1983). The crust is interpreted to be thinned upper lithosphere due to restricted magma supply towards the ends of spreading segments bounded by juxtaposed cold crust of the transform (White *et al.*, 1984). The second type of thinned crust is characterized by thickness of 3 km or less, low seismic velocities, high velocity gradients, and occurs both at small- and large-offset fracture zones (e.g., Kane, Oceanographer, and unnamed small offset North Atlantic fracture zone) (Sinha and Loudon, 1983).

Cormier *et al.* (1984) showed that 2–3 km thick crust, characterized by low seismic velocities, high velocity gradients, and an absence of the oceanic layer 3 refractor, is common along a 250 km long, 10–15 km wide path of the Kane Fracture Zone east of its active transform. This type of crust, whose

mechanism of formation is uncertain, may be a serpentinized volcanic or plutonic lid of mafic and ultramafic rocks, or highly fractured and brecciated basement rocks (Detrick *et al.*, 1982; Sinha and Loudon, 1983). Sinha and Loudon (1983) hypothesized that such crust may form below a critical spreading rate where normal crustal magmatic processes cease at ridge-transform intersections; thus thin, fractured, and hydrothermally altered ultramafic crust might be produced, lying directly on top of unaltered upper mantle. In any case, the lower density of this anomalous crust in a fracture zone trough should cause a geoid anomaly that is superimposed on the geoid anomaly caused by the uncompensated basement topography; thus the geoid height/topography ratio would be amplified where the low density crust was present. For example, extremely high values for the geoid height/topography ratio of about 25 cm km^{-1} in profiles 3e and 4e, east of the active transform, may reflect anomalously low density crust beneath the fracture valleys.

The cross correlation results (Figures 10–19) show clearly that geoid undulations with wavelengths less than 100 km to a first approximation are well correlated to basement topography. Observed horizontal offsets, or mismatches, between the basement and geoid expression of the Kane Fracture Zone can be due to several factors: (1) inaccuracies in the basement profiles, (2) effects of out-of-plane basement features, and (3) density variations in the crust and upper mantle.

Because location of basement features along the older, sediment-covered parts of the Kane Fracture Zone is controlled only by seismic reflection profiles (sometimes widely spaced), inaccuracies of several kilometers and more are likely (Tucholke and Schouten, 1988). Nearer the Kane transform, sediment cover thins and basement features are well located (<1–2 km) by multibeam bathymetry. These observations are reflected by the generally decreasing mismatch between basement and geoid with decreasing age (Figures 8, 9). As expected, the most pronounced mismatches are for crustal ages greater than about 130 Ma (profiles 17 w to 20 w, Figures 8–10) where the amplitudes of the geoid signals are well above the noise level (3–10 cm vs. 0.7 cm), but seismic reflection control on basement structure is limited.

Qualitative examination of geoid tracks with respect to high-amplitude, out-of-plane basement features indicates that there are generally small but noticeable effects on the geoid profile. The resulting mismatches with basement topography are most recognizable away from the fracture zone, where the dominant basement structure is abyssal hills that are subparallel to the satellite tracks. Mismatch at the fracture valley, where structural fabric is strongly lineated *across* the tracks, generally is negligible.

On young ocean crust, where basement structure is well controlled, observed mismatches between the basement and geoid expression across the fracture zone must be due to density variations in the crust. One of the best examples is a distinct phase shift (~15 km) between geoid and basement topography directly east of the active transform of the Kane Fracture Zone (Profile 1e, Figure 15). This observation is consistent with a phase offset of 15–20 km between gravity and bathymetry in the same area (Abrams *et al.*, 1988). The offset is caused by presence of a transverse ridge on the north side of the fracture valley. Tucholke and Schouten (1988) interpreted formation of the ridge to be a result of two co-occurring processes. The first was a counterclockwise change in spreading direction ('extensional' for Kane transform) that began about 22 Ma and resulted in a tendency for spreading-ridge tips to propagate into and uplift the opposing transform walls at the ridge-transform intersections. The second process was the overall southward movement of the Mid-Atlantic Ridge plate-boundary relative to subaxial

melting anomalies linked to a deeper, mesospheric reference frame; this 'absolute' motion accentuated northward propagation of the eastern spreading axis and uplift of the old transform wall while nullifying similar propagation and uplift at the western ridge-transform intersection. The positive Bouger gravity anomaly over the transverse ridge and the northern part of the fracture valley appears to be explained best by a 20–30 km wide upwarp of the Moho beneath the isostatically uncompensated transverse ridge (Abrams *et al.*, 1988).

Similar transverse ridges were identified by Tucholke and Schouten (1988) between 32° and 37° W along the northern wall of the eastern limb of the Kane Fracture Zone. The transverse ridge is clearly visible in profiles 8e and 9e over 72 and 79 MA crust (Figures 17). The geoid signal of profile 8e shows a phase shift relative to the fracture valley that is only about half of that in profile 1e, but it is comparable to the phase shift in profile 2e which also crosses the younger transverse ridge. Profile 9e shows no significant phase shift, although the basement structure on this profile is complicated by an additional transverse ridge and two additional fracture zone troughs. Taken together, profiles 8e and 9e suggest that any upwarp of the Moho is attenuated in comparison to that beneath the transverse ridge just east of the present transform. Either the upwarp was never well developed, or lithospheric aging has decreased its effect.

The three parallel fracture valleys east of profile 8e formed during a counterclockwise change in spreading direction that began about 92 Ma, prior to chron 34 (Tucholke and Schouten, 1988). Two of the Geosat profiles (9e, 10e; Figure 17) examined here cross this area. The geoid trough of profile 9e correlates well with the southernmost fracture valley. The northernmost valley, however, which has basement expression and minor sediment fill similar to the southern valley, has a negligible geoid signature. According to Tucholke and Schouten's (1988) model of fracture-zone response to the change in plate motion, crustal ages of the central and northern fracture valley are progressively older than that of the southern valley, and both became defunct in crust 2 to 6 m.y. younger than that of the profile 9e crossing. It seems unlikely that the slightly greater crustal ages in the northern valleys would have much effect on their geoid expression. It is possible, how-

ever, that there were fundamental differences in lithospheric accretion parameters along the two northern fracture valleys, ultimately reflected in their demise and in lateral density variations that could explain the observed geoid. More closely spaced geoid/gravity data are needed to constrain the possible explanations.

In contrast to profile 9e, profile 10e (86 Ma crust) shows the geoid trough correlating with the northern fracture valley (the central and northern valleys are merging at this point), and the southern valley exhibits a small basement trough with a slight geoid deflection (Figure 17). The central and southern valleys at this location are interpreted to have formed by shearing through older crust at the time of change in plate motion (Tucholke and Schouten, 1988). Their consequent low-amplitude basement expression and the likely absence of any large intracrustal density variations are thought to explain the lack of a significant corresponding geoid anomaly. The northern valley, however, formed prior to the change in plate motion, and it is characterized by a much deeper basement trough and a clear geoid low.

Another profile that crosses a pair of fracture valleys is profile 12e farther east (Figures 2, 18). Both valleys are sediment filled. The northern valley was formed by crustal accretion in the domain of a ridge-transform intersection, but the southern valley formed as an adjustment fracture which sheared through old crust following a geologically abrupt clockwise shift in plate motion about 100–102 Ma (Tucholke and Schouten, 1988). The northern valley is deep and shows a correlative geoid trough. The southern valley is of comparable depth, but has no geoid signature. Like profile 10e, the sheared lithosphere apparently has little density variation compared to adjacent normal crust, and it therefore is not reflected in the geoid. The lack of a geoid trough in these profiles (and over the central and northern valleys in profile 9e) provides clear evidence that upper-lithosphere density variations must have an effect on the short-wavelength geoid. Thus while linear geoid lows provide a first approximation to fracture-valley position and orientation, they are not always diagnostic, particularly if changes in plate motion have caused adjustment fractures to form.

Up to this point, we have considered mainly the large-scale mismatches between geoid and basement

topography. However, subtler effects also may be present. For a large-offset fracture zone such as the Kane, even small plate-motion changes can cause propagation or retreat of spreading-ridge tips at ridge-transform intersections and thus cause restructuring of crustal accretion and faulting in the fracture valley. We can expect that as these patterns propagate or retreat across the valley they also will cause cross-valley shifts in lithosphere density. These shifts should appear as offsets between basement depth and geoid trough.

The two limbs of the Kane Fracture Zone clearly record long-period changes in relative plate motion (Figure 2). For example, from about 59 to 22 Ma, the Kane transform generally was in compression (ridge-tip retreat), compared to extensional plate-motion changes during the periods 92 to 59 Ma and 22 Ma to present (Tucholke and Schouten, 1988). If the above argument is correct, we should be able to see some long-period changes in offset between geoid and basement depth that correlate with the extensional and compressional episodes. Examination of Figures 8 and 9 show that this is not the case. There are several possible explanations. One is that the geoid is reflecting density variations that are simply real 'geologic noise'. Another possibility is that the wide spacing of Geosat tracks has created an aliasing problem. Examination of fine-scale structure of the Kane Fracture Zone suggests that within the larger episodes of transform compression or extension, there are small but more rapid plate motion changes (1–3 m.y.) and associated changes in the nature of crustal formation at ridge-transform intersections (Tucholke and Schouten, 1988). Under these conditions, the average profile spacing of Geosat (165 km at the equator = 5–15 m.y.) would sample only widely spaced random changes in basement structure, and thus in offset between geoid and basement troughs. Finally, the 'absolute motion' of the plate boundary could cause density variations to shift across the transform valley, causing not only variations in time along-strike, but also asymmetries between fracture-zone limbs. It will require analysis of closely-spaced satellite profiles to distinguish among these possibilities.

As Figure 6 and Figures 11–19 indicate, there are many geoid anomalies adjacent to the Kane Fracture Zone that have signals comparable to or even larger than the Kane fracture valley, but they are not

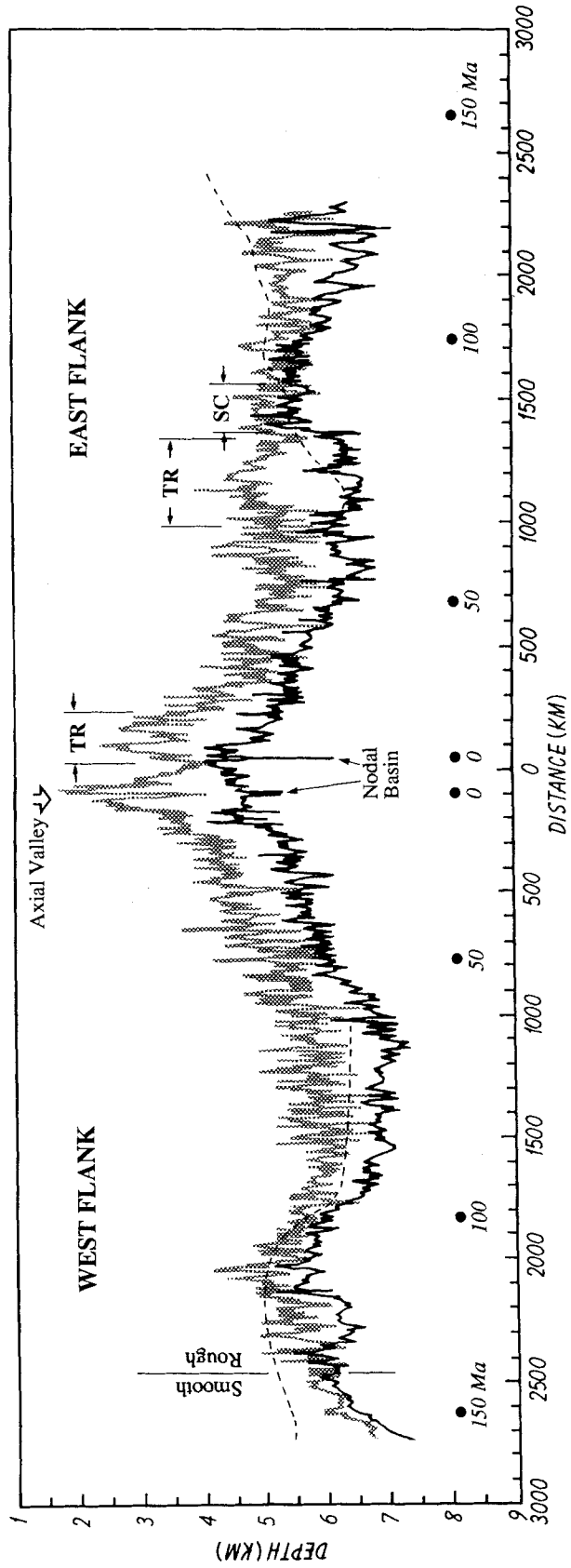


Fig. 20. Profiles of basement topography along the axis of the Kane Fracture Zone (solid line) and along minimum depths of adjacent crust just north of the fracture zone (shaded). The dashed lines are sea-floor profiles that show sediment infill of the fracture zone. Locations of the axial valley on the northern profile and the two nodal basins on the axial profile are indicated. 'TR' locates transverse ridges on the northern profile, and 'SC' shows the position of old crust that was sheared during reorganization of the transform geometry in response to a change in plate motion ca. 92-90 Ma. The rough/smooth crustal boundary (Sundvik *et al.*, 1984) is indicated. Crustal ages on the young side of the fracture zone are shown in the lower part of the figure. The figure is adapted from Tucholke and Schouten (1988).

related to major fracture zones. This observation raises the question of whether we would be able to identify such fracture zones from their geoid signals alone. In this paper we have discussed descending Geosat tracks. Use of complete sets of ascending and descending geoid profiles would significantly improve identification of the curvilinear fracture-zone trends and trajectories and would generally distinguish them from localized geoid high or lows. The continuity and generally good predictability of fracture zones over relatively large distances aids this process, even when the identification of a fracture zone in a single geoid profile might otherwise be difficult. Examples of this are studies by Shaw (1987) and Shaw and Cande (1990), who used geoid data to identify and map fracture zone trajectories in the South Atlantic. However, in areas where fracture-zone structure is other than normal (e.g., where structural modifications have occurred in response to plate-motion changes), the geoid signals are inadequate to resolve the actual fracture zone traces and thus the causes of the structural variability.

Conclusions

This study shows that short-wavelength geoid height (wavelengths 25–100 km) to a first approximation is highly correlated with the basement topography over the Kane Fracture Zone. The observed mismatches can be categorized into two classes: a) poorly correlated profiles over older crust (130–160 Ma), and b) clearly defined offsets (0–15 km, mostly < 10 km) between geoid and basement troughs over most of the length of the fracture zone. The first class of mismatches is most readily explained by lack of control on basement depth along the subsatellite tracks considered.

The second class of mismatches shows separations of geoid and basement troughs that are best explained by crustal and subcrustal density variations. The largest mismatch, ≈ 15 km, is observed over the transverse ridge east of the active Kane transform. It is interpreted to be caused by a 20–30 km wide upwarp of the Moho under the transverse ridge and the northern part of the fracture valley (Abrams *et al.*, 1988). Phase shifts between the topographic and geoid expression of the fracture-zone valley are 12 km or less for all remaining profiles with a majority showing phase shifts of 9 km or less. Hence the

filtered short-wavelength geoid between 25 and 100 km allows us to map the axis of a major portion of the Kane Fracture Zone to within less than 10 km, with an average mismatch between fracture-zone valley and geoid trough of about 5 km.

A lack of any geoid depression over certain basement troughs was found in regions where large changes in direction of plate motion occurred and were accommodated by major adjustments in fracture-zone structure. Examples are observed in two fracture valleys formed by shearing through older crust along adjustment fractures on the eastern Kane Fracture Zone (profiles 10e and 12e; Figures 17 and 18). Lack of geoid expression over two well-defined troughs apparently formed by 'normal' crustal accretion at ridge-transform intersections is also observed in this domain (profile 9e; Figure 17), but the causal mechanism and lithospheric structure are uncertain.

The excellent correlation between geoid wavelengths of 25 to 100 km and uncompensated basement topography should allow determination of a transfer function between geoid and basement topography. Then satellite altimetry data could be used to approximate bathymetry from the high-frequency geoid. In the future, filtered geoid heights derived from stacked deflection-of-the-vertical data from Geosat can be used with confidence to map fracture zones in regions with sparse bathymetric data-coverage, such as in remote high southern latitudes. However, geoid expression of fracture zones is complex and still not fully understood over areas where large-offset transforms have experienced significant reorientations in response to plate-motion changes. In these areas caution must be exercised attempting to define fracture-zone structure beyond general trends.

Acknowledgements

We would like to thank Lisa M. Gahagan and two anonymous reviewers for constructive comments on the manuscript. Financial support for this project was provided by Amoco International Oil Co., Chevron Overseas Petroleum Co., Conoco, Elf Aquitaine, Exxon Production Research, Mobil Oil Co., Petro-Canada, Phillips Petroleum and Shell Development Co. as part of their sponsorship of the Paleocyanographic Mapping Project at the University of Texas at Austin. At Woods Hole Oceanographic Institution, this research was supported by

ONR Contract N00014-87-K-0007 and NSF grants OCE-8716713.00 and OCE-8812490.

References

- Abrams, L. J., Detrick, R. S., and Fox, P. J., 1988, Morphology and Crustal Structure of the Kane Fracture Zone Transverse Ridge, *J. Geophys. Res.* **93**, 3195–3210.
- Collette, B. J., 1974, Thermal Contraction Joints in a Spreading Seafloor as Origin of Fracture Zones, *Nature* **251**, 299–300.
- Collette, B. J., 1986, Fracture Zones in the North Atlantic: Morphology and a Model, *J. Geophys. Soc. London* **143**, 763–774.
- Collette, B. J., Slootweg, A. P., Verhoef, J., and Roest, W. R., 1984, Geophysical Investigations of the Floor of the Atlantic Ocean between 10° and 38° N (Kroonvlag-project), *Proc. Kon. Ned. Akad. Wet.* **87**, (series B), 1–76.
- Cormier, M. -H., Detrick, R. S., and Purdy, G. M., 1984, Anomalous Thin Crust in Oceanic Fracture Zones: New Seismic Constraints from the Kane Fracture Zone, *J. Geophys. Res.* **89**, 10249–10266.
- Detrick, R. S., Cormier, M. H., Prince, R. A., and Forsyth, D. W., 1982, Seismic Constraints of the Crustal Structure within the Vema Fracture Zone, *J. Geophys. Res.* **87**, 10599–10612.
- Fox, P. J. and Gallo, D. G., 1984, A Tectonic Model for the Ridge-Transform-Ridge Plate Boundaries: Implications for the Structure of Oceanic Lithosphere, *Tectonophysics* **104**, 205–242.
- Fox, P. J. and Gallo, D. G., 1986, The Geology of the North Atlantic Transform Plate Boundaries and their Aseismic Extensions, in Vogt, R. and Tucholke, B. E. (eds.), *The Geology of North America, Vol. M*, The Western North Atlantic Region, *Geol. Soc. Am.*, 157–172.
- Francheteau, J., Choukroune, P., Hekinian, R., Le Pichon, X., and Needham, H. D., 1976, Oceanic Fracture Zones do not Provide Deep Sections in the Crust, *Can. J. Earth Sci.* **13**, 1223–1235.
- Gahagan, L. M., Scotese, C. R., Roger, J. -Y., Sandwell, D. T., Winn, J. K., Tomlins, R. L., Ross, M. I., Newman, J. S., Müller, R. D., Mayes, C. L., Lawver, L. A., and Heubeck, C. E., 1988, Tectonic Fabric Map of the Ocean Basins from Satellite Altimetry Data, *Tectonophysics* **155**, 1–26.
- GEBCO, 1978, General Bathymetric Chart of the Oceans, Sheet 5.04, Hydrographic Chart Distribution Office, Ottawa.
- Kent, D. V. and Gradstein, F. M., 1986, A Jurassic to Recent Chronology, in Vogt, R. and Tucholke, B. E. (eds.), *The Geology of North America, Vol. M*, The Western North Atlantic Region, *Geol. Soc. Am.*, 45–50.
- Klitgord, K. D. and Schouten, H., 1986, Plate Kinematics of the Central Atlantic, in Vogt, R. and Tucholke, B. E. (eds.), *The Geology of North America, Vol. M*, The Western North Atlantic Region, *Geol. Soc. Am.*, 351–404.
- Louden, K. E. and Forsyth, D. W., 1982, Crustal Structure and Isostatic Compensation near the Kane Fracture Zone from Topography and Gravity Measurements – 1. Spectral Analysis Approach, *Geophys. J. R. astr. Soc.* **68**, 725–750.
- Marks, K. M. and Sailor, R. V., 1986, Comparison of Geos-3 and Seasat Altimeter Resolution Capabilities, *J. Geophys. Res.* **13**, 697–700.
- Marsh, J. G. and Martin, T. V., 1982, The Seasat Altimeter Mean Surface Model, *J. Geophys. Res.* **87**, 3269–3280.
- MacArthur, J. L., Marth, Jr., P. C., and Wall, J. G., 1987, The Geosat Radar Altimeter. *John Hopkins APL Technical Digest* **8**, 176–181.
- MacDonald, K. C., 1986, The Crest of the Mid-Atlantic Ridge: Models for Crustal Generation Processes and Tectonics, in Vogt, R. and Tucholke, B. E. (eds), *The Geology of North America, Vol. M*, The Western North Atlantic Region, *Geol. Soc. Am.*, 51–68.
- McConathy, D. R. and Kilgus, C. C., 1987, The Navy Geosat Mission: An Overview. *John Hopkins APL Technical Digest* **8**, 234–244.
- McKenzie, D. and Bowin, C., 1976, The Relationship between Bathymetry and Gravity in the Atlantic Ocean, *J. Geophys. Res.* **81**, 1903–1915.
- Olivet, J.-L., LePichon, X., Monti, S., and Sichel, B., 1974, Charlie-Gibbs Fracture Zone, *J. Geophys. Res.* **79**, 2059–2072.
- Pockalny, R. A., Detrick, R. S., and Fox, P. J., 1988, Morphology and Tectonics of the Kane Transform from Sea Beam Bathymetry Data, *J. Geophys. Res.* **93**, 3179–3193.
- Potts, C. G., Williams, C. A., Calvert, A. J., and White, R. S., 1986, The Tydemann: Morphology and Seismic Structure of Old Fracture Zone Crust, *J. Geol. Soc., Lond.* **143**, 833–843.
- Press, W. H., Flannery, B. P., Teukolsky, S. A., and Vetterling, W. T., 1986, *Numerical Recipes*, Cambridge University Press, 818 pp.
- Roest, W. R., 1987, Seafloor Spreading Pattern of the North Atlantic between 10° and 40° N, *Geological Ultralectina*, No. 48, 121 pp.
- Roest, W. R. and Collette, B. J., 1986, The Fifteen Twenty Fracture Zone and the North American-South American Plate Boundary, *J. Geol. Soc., Lond.* **143**, 833–843.
- Sandwell, D. T., 1984, Thermomechanical Evolution of Oceanic Fracture Zones, *J. Geophys. Res.* **89**, 11401–11413.
- Sandwell, D. T. and Schubert, G., 1982, Lithospheric Flexure at Fracture Zones, *J. Geophys. Res.* **87**, 4657–4667.
- Sandwell, D. T. and McAdoo, D. C., 1988, Marine Gravity of the Southern Ocean and Antarctic Margin from Geosat, *J. Geophys. Res.* **93**, 10389–10396.
- Sandwell, D. T. and McAdoo, D. C., 1990, High Accuracy High-Resolution Gravity Profiles From 2 Years of the Geosat/ERM, *J. Geophys. Res.*, 3049–3060.
- Sinha, M. C. and Loudon, K. E., 1983, The Oceanographer Fracture Zone – I. Crustal Structure from Seismic Refraction Studies, *Geophys. J. R. astr. Soc.* **75**, 713–736.
- Sundvik, M., Larson, R. L. and Detrick, R. S., 1984, Rough-Smooth Basement Boundary in the Western North Atlantic Basin: Evidence for a Seafloor-Spreading Origin, *Geology* **12**, 31–34.
- Tucholke, B. E., Houtz, R. E., and Ludwig, W. J., 1982, Sediment Thickness and Depth to Basement in Western North Atlantic Ocean Basin, *Amer. Ass. Pet. Geol. Bull.* **66**, 1384–1395.
- Tucholke, B. E. and Schouten, H., 1988, Kane Fracture Zone, *Marine Geophys. Res.* **10**, 1–39.
- Turcotte, D. L., 1974, Are Transform Faults Thermal Contraction Cracks?, *J. Geophys. Res.* **79**, 2573–2577.
- Twigt, W., Verhoef, J., Rohr, K., Mulder, Th. F. A., and Collette, B. J., 1983, Topography, Magnetism and Gravity Over the Kane Fracture Zone in the Cretaceous Quiet Zone (African Plate). *Proc. Kon. Ned. Akad. Wet.* **86**, (Series B), 181–210.
- Van Andel, Tj. H., 1971, Fracture Zones, Comments on Earth Sciences, *Geophysics* **1**, 159–166.
- Vogt, P. R., Zondek, B., Fell, P. W., Cherkis, N. Z., and Perry, R. K., 1984, Seasat Altimetry, the North Atlantic Geoid, and Evaluation by Shipborne Subsattellite Profiles, *J. Geophys. Res.* **89**, 9885–9903.
- White, R. S., Detrick, R. S., Sinha, M. C., and Cormier, M. H., 1984, Anomalous Seismic Crustal Structure of Oceanic Fracture Zones, *Geophys. J. Roy. Astron. Soc.* **79**, 779–98.